

# Magnetic Fields in Massive Star Forming Regions

R. L. Curran<sup>1,2\*</sup>, and A. Chrysostomou<sup>2,3</sup>

<sup>1</sup>*School of Cosmic Physics, Dublin Institute for Advanced Studies, 5 Merrion Square, Dublin 2, Ireland*

<sup>2</sup>*School of Physics, Astronomy & Maths, University of Hertfordshire, College Lane, Hatfield, Herts., AL10 9AB, UK*

<sup>3</sup>*Joint Astronomy Centre, 660 N. A'ohoku Place, University Park, Hilo, Hawaii 96720, U.S.A.*

Accepted —; Received —

## ABSTRACT

We present the largest sample of high-mass star-forming regions observed using sub-millimetre imaging polarimetry. The data were taken using SCUBA in conjunction with the polarimeter on the JCMT in Hawaii. In total, 16 star forming regions were observed, although some of these contain multiple cores. The polarimetry implies a variety of magnetic field morphologies, with some very ordered fields. We see a decrease in polarisation percentage for 7 of the cores. The magnetic field strengths estimated for 14 of the cores, using the corrected CF method, range from  $<0.1$  mG to almost 6 mG. These magnetic fields are weaker on these large scales when compared to previous Zeeman measurements from maser emission, implying the role of the magnetic field in star formation increases in importance on smaller scales. Analysis of the alignment of the mean field direction and the outflow directions reveal no relation for the whole sample, although direct comparison of the polarimetry maps suggests good alignment (to at least one outflow direction per source) in 7 out of the 15 sources with outflows.

**Key words:** Techniques: polarimetric – stars: formation – stars: magnetic fields – submillimetre

## 1 INTRODUCTION

One of the remaining problems yet to be understood within star formation is the collapse of a cloud into a star, and the relatively slow star formation rate observed. This problem suggests there is some form of support preventing the clouds from collapse (at least initially). For instance, if typical ( $M \sim 10^{3-4} M_{\odot}$ ) molecular clouds had no support, and so were in free-fall collapse, with all the mass going into stars, cloud lifetimes would be unrealistically short, and the star formation rate would be up to three orders of magnitude greater than observed (Mouschovias 1976). Thermal pressure is weak compared to the gravitational stresses in the cloud, so the support may come from the magnetic field that permeates the gas or the pressure of turbulent eddies – indeed it is likely that these two mechanisms are coupled.

Spinning elongated dust grains in such star forming regions can become aligned to the local magnetic field, such that the grains' semi-major axes are perpendicular (on average) to the magnetic field lines. The net thermal emission from such grains is polarised (perpendicular to the direction of the magnetic field lines), and can be used to trace the morphology of the magnetic field as seen projected onto the plane of the sky. Further information can be gained on the magnetic field via Zeeman split-

ting (Sarma, Troland & Romney 2001), which yields the line of sight magnetic field strength. Ion/neutral linewidths (Houde et al. 2000), can also be used to gain information on the orientation of the magnetic field.

In order to understand the importance of the magnetic field on large scales, consistent with tracing the magnetic field in the envelope of these cores, we present SCUBA 850 $\mu$ m imaging polarimetry of 20 star forming cores. We also introduce a new, improved (more representative) method of data reduction for SCUBA polarimetry, which presents the errors in polarisation in a truer light. We discuss the implied magnetic field morphology across the cores, as well as the estimated field strength for some of the regions using the modified Chandrasekhar & Fermi (1953, henceforth CF) method. We use this estimate to indicate the importance of the magnetic field on these scales on the support of these clouds, and compare the mean magnetic field direction to the outflow directions, to see if they correspond in the plane of the sky.

## 2 OBSERVATIONS & DATA REDUCTION

The sample of high-mass star-forming regions were selected from the Arcetri water maser atlas (Comoretto et al. 1990; Brand et al. 2001) based on the following criteria: i) well known and studied star-forming regions, ii) varied morpholo-

\* E-mail: rcurran@cp.dias.ie

gies, iii) submillimetre bright (Jenness, Scott & Padman 1995); and iv) observable from the JCMT in Hawaii (i.e.  $-40^\circ \leq \delta \leq +70^\circ$ ).

The observations took place over several nights between 1998 May 16 and 2000 October 10 at the James Clerk Maxwell Telescope (JCMT) in Hawaii. The Submillimetre Common User Bolometer Array (SCUBA) (Holland et al. 1999) was used in conjunction with the polarimeter – consisting of a rotating quartz half-wave retarder ahead of a fixed wire-grid analyser; Greaves et al. (2003) – which was mounted on the entrance window to SCUBA. The Jiggle-mapping mode of observation was used, involving ‘jiggling’ the secondary mirror to fully sample the beam. Sixteen different positions (1 second exposures at each) are required to fully sample the map – these positions have a separation of  $6.18''$  for the Long-Wavelength ( $850\mu\text{m}$ ) array. The secondary mirror performed the usual chop during the jiggle pattern to provide atmospheric cancellation. The nod was carried out over periods of around 10-20 seconds to eliminate slowly varying sky gradients.

The polarimeter complicates the normal observing procedure such that complete 16-point jiggle maps are required at specific positions of the half-wave retarder, each separated by  $22.5^\circ$ . Therefore 16 jiggle maps are observed to complete one cycle of the retarder. The direction of the chop-throw was decided based on the morphology of the target.

The data reduction was carried out using the routines from the SCUBA User Reduction Facility (SURF) (Jenness & Lightfoot 1998) to reduce the SCUBA images and routines from POLPACK (Berry & Gledhill 2001) were used to reduce the polarimetry. The nod and chop of the telescope were corrected for and the flat-field applied to the observations in the standard manner. The atmospheric extinction was calculated based on the start and end times of each observation: throughout the night the Caltech Submillimetre Observatory (CSO) phase monitor measures the  $\tau_{225\text{GHz}}$  (or  $\tau_{\text{CSO}}$ ), and a polynomial was fitted to the measured points. This polynomial was then applied to the start and end times of the observation to calculate the  $\tau_{\text{CSO}}$  for the observation and converted into  $\tau_{850\mu\text{m}}$  using:

$$\tau_{850\mu\text{m}} = 3.99 \times (\tau_{\text{CSO}} - 0.004) \quad (1)$$

for the data taken before October 2000, and:

$$\tau_{850\mu\text{m}} = 4.02 \times (\tau_{\text{CSO}} - 0.001) \quad (2)$$

for the data taken during and after October 2000. The extinction is assumed to vary linearly throughout the observation. The airmass at which each bolometer measurement was made is calculated then multiplied by the zenith sky extinction. Each data point was then multiplied by the exponential of the optical depth to give the value that would have been measured in the absence of the atmosphere. Bolometers which were deemed excessively noisy were switched off at this point in the data reduction. The sky noise was removed using bolometers that had no significant flux from the source. The average (mean) flux from these bolometers was assumed to come from sky emission, and was subtracted from all of the bolometers in order to remove the sky signal. The instrumental polarisation was removed in the usual manner. The data were re-gridded using a Gaussian weighting function, with the scale set to  $7''$  (half the beamsize).

**Table 1.** Table of flux calibrators and flux calibration factors.

Date	Flux Calibrator	FCF Jy/arcsec <sup>2</sup> /V
19980516	Uranus	2.35
19990620	Uranus	2.02
19990705	Uranus	2.21
19990706	Saturn	1.81
20001006	Uranus	1.96
	CRL2688	1.72
20001010	CRL2688	1.71

The pixel size was set to  $6.18''$ , matching the jiggle pattern, in order to calculate the polarimetry vectors accurately.

POLPACK packages are then used to calculate the Stokes parameters by fitting the following curve (Sparks & Axon 1999) to the data:

$$I'_k = \frac{t}{2}(I + \epsilon(Q \cos 2\phi_k + U \sin 2\phi_k)) \quad (3)$$

where  $I'_k$  is the expected intensity in image  $k$ ,  $t$  is the wire-grid analyser transmission factor,  $\epsilon$  is the analyser polarising efficiency factor and  $\phi_k$  is the effective retarder position angle after correction for the parallactic angle for image  $k$ . The polarisation percentage and position angles of the vectors are then calculated from the Stokes parameters, without any binning. The catalogue was clipped such that noisy polarisation vectors were not included. The clipping used was  $I > 0$  and  $dP < 0.75$ . For 3% polarisation, this represents a maximum position angle error of  $7.15^\circ$ . It was chosen to clip the vectors on polarisation errors instead of signal-to-noise, as clipping on the latter would result in disposing of points where the polarisation is low or zero, both of which are perfectly valid measurements.

Finally, flux calibration (Jenness et al. 2002) was carried out using observations of Uranus, Saturn and CRL2688. The flux calibration factors (FCFs) are listed in table 1. These FCFs were applied to the data, with any objects observed over more than one night having the data for each night reduced separately, then the flux calibrated images co-added to create the final image.

## 2.1 Pixel Size

Since the introduction of SCUBA on the JCMT, it has become “standard” to reduce  $850\mu\text{m}$  data with a pixel spacing of  $3.09''$ . This is mainly due to a  $3.09''$  jiggle-step being required to fully sample the beam at  $450\mu\text{m}$ . This allowed for easier comparisons between  $450\mu\text{m}$  and  $850\mu\text{m}$  data. The method of data reduction naturally continued when the polarimeter was introduced.

Careful inspection of data reduced by this method (pixel size set to  $3.09''$  and with  $2 \times 2$  binning of vectors) and reduced using a pixel size of  $6.18''$  with no binning, revealed significant differences in the number of vectors. The polarisation errors in the latter reduction were higher than those in the first reduction method, resulting in a decrease in the number of vectors selected after error clipping.

The change in the errors in polarisation are due to the binning. When the pixel size is set to  $3.09''$ , four pixels are produced for every one when the size is  $6.18''$ . A vector is

then produced for each pixel, with the vectors for the smaller pixels being binned together — adding the polarisations together in quadrature to calculate the error. This erroneously reduces the resultant errors.

The observing mode used means that one independent polarisation measurement is taken at steps of every  $6.18''$ , the results of which can be superimposed over an intensity image created with  $3.09''$  pixels.

### 3 CORE PROPERTIES

#### 3.1 Core Masses

The mass of the star-forming cores can be calculated by assuming:

$$M_{\text{Total}} = \frac{gS_{\nu}d^2}{\kappa_{\nu}B_{\nu}(T_{\text{dust}})} \quad (4)$$

where  $g$  is the gas-to-dust ratio,  $S_{\nu}$  is the flux,  $d$  the distance,  $\kappa_{\nu}$  the absorption coefficient at frequency  $\nu$ , and  $B_{\nu}(T_{\text{dust}})$  is the Planck function for frequency  $\nu$  at a temperature of  $T_{\text{dust}}$ .

Using a gas-to-dust ratio of 100:1 (Hildebrand 1983), and an absorption coefficient of  $0.15 \text{ m}^2 \text{ kg}^{-1}$  estimated from Ossenkopf & Henning (1994) based on a number density of  $n_H = 10^5 \text{ cm}^{-3}$ , thick ice mantles and a formation timescale of  $10^5$  years, mass estimates for the cores were calculated (listed in table 2, along with the other parameters derived from the observations).

The mass of these objects are subject to uncertainties within the used parameters, especially any errors in measuring the distance to the core. The gas-to-dust ratio, which may be as low as 45:1 (McCutcheon et al. 1995) also introduces an error that may be up to a factor of 2. The absorption coefficient at  $850\mu\text{m}$  still has not been determined precisely (Hildebrand 1983; Chini et al. 2001), although the value adopted in this paper from Ossenkopf & Henning (1994) agrees with the values determined by Bianchi et al. (2003) and Visser et al. (2002). The masses we determine in this paper are therefore the upper limits for the temperature of the cores.

#### 3.2 The Magnetic Field Strength

The CF relation can be used to obtain the plane of the sky average magnetic field strength. This method is based on equipartition and the ability of the magnetic field to retain straight field lines under the influence of turbulence. The plane of the sky average field strength can be calculated via:

$$\langle B_{\text{pos}} \rangle = f \sqrt{4\pi\rho \frac{\sigma_{v_{\text{los}}}}{\sigma_{\theta}}} \quad G, \quad (5)$$

where  $\rho$  is the mean density ( $\text{g cm}^{-3}$ ),  $\sigma_{v_{\text{los}}}$  the line of sight velocity dispersion ( $\text{cm s}^{-1}$ ),  $\sigma_{\theta}$  is the dispersion in polarisation position angles (measured east of north) and is corrected for measurement errors ( $\sigma_{\theta}^2 = \sigma_{\text{measured}}^2 - \sigma_{\text{error}}^2$ ) where  $\theta$  is in radians, and  $f$  is a correction factor found to be  $\sim 0.5$  (Heitsch et al. 2001).

Errors on the position angle of the vectors are calculated based on the polarimetry signal-to-noise:

$$d\theta = \frac{28.6^\circ}{s_p} \quad (6)$$

where  $d\theta$  is the error in the position angle and  $s_p$  is the signal-to-noise in the polarisation. Therefore in regions where the polarisation percentage is low (e.g. across the main core of DR21(OH)), then  $\sigma_{\text{meas}} \sim \sigma_{\text{err}}$  resulting in misleadingly small dispersion angles, and very strong magnetic fields. By only selecting the vectors which have a signal-to-noise (in polarisation) of  $> 3$ , this problem is avoided, therefore all of the magnetic field strength estimates in this paper are based on vectors selected in this way. Please note, however, as mentioned earlier, the vectors shown in the figures are not selected in this way, as in terms of magnetic field morphology, polarisation nulls and low levels of polarisation are valid detections.

The CF method should be used with caution when calculating the magnetic field strength in the plane of the sky. The  $15''$  beam-size of the JCMT means that the small-scale tangling of the magnetic field field can occur within the beam, and so the measured vectors only represent the net magnetic field direction, leading to over-estimates of the field strength. Modelling studies of this effect (Heitsch et al. 2001) have lead to the introduction of a correction factor  $f$ , which has been found to be  $\sim 0.5$  (see eq. 5). Also, any underlying magnetic field morphology (e.g. intrinsic field curvature) has not been accounted for in calculating the dispersion in position angles of the polarimetry vectors (i.e. this technique assumes *a priori* that the magnetic field is uniform).

Uncertainties in our estimations of the magnetic field strength arise from calculating the density of the cores, which incorporates the errors involved in calculating the mass, they therefore represent the upper limits of the magnetic field strength. There are also errors in calculating the volume of the core which contribute as a spherical geometry has been assumed for each core (except where otherwise stated), although with no density tracer information, we lack the ability to modal the three-dimensional structure of the cores, therefore the upper limits stated are solely for spherical geometry. The velocity of the gas within the core introduces another error as a FWHM of  $\sim 2 \text{ kms}^{-1}$  has been used but it may be anywhere between  $1 \text{ kms}^{-1}$  and  $3 \text{ kms}^{-1}$  (Brand et al. 2001; Thompson et al. 2004). Measurement errors are also introduced by the angle  $\theta$ , although these are relatively small in comparison to the other errors stated.

## 4 INDIVIDUAL CORES

### 4.1 Cepheus A

Cepheus A is a well-known star forming region. Located at a distance of  $\sim 730 \text{ pc}$  (Blaauw, Hiltner & Johnson 1959), it is the closest star-forming region in the sample. The region contains many signatures of massive star formation such as: a) a sub-mm source (observed here) with a total luminosity of  $2.5 \times 10^4 L_{\odot}$  (Koppenaal et al. 1979; Evans et al. 1981), b) a cluster of 14 compact radio continuum sources (Beichman, Becklin & Wynn-Williams 1979; Hughes & Waterlout 1984), c) clusters of  $\text{H}_2\text{O}$  and OH masers (Lada et al. 1981; Migenes, Cohen & Brebner

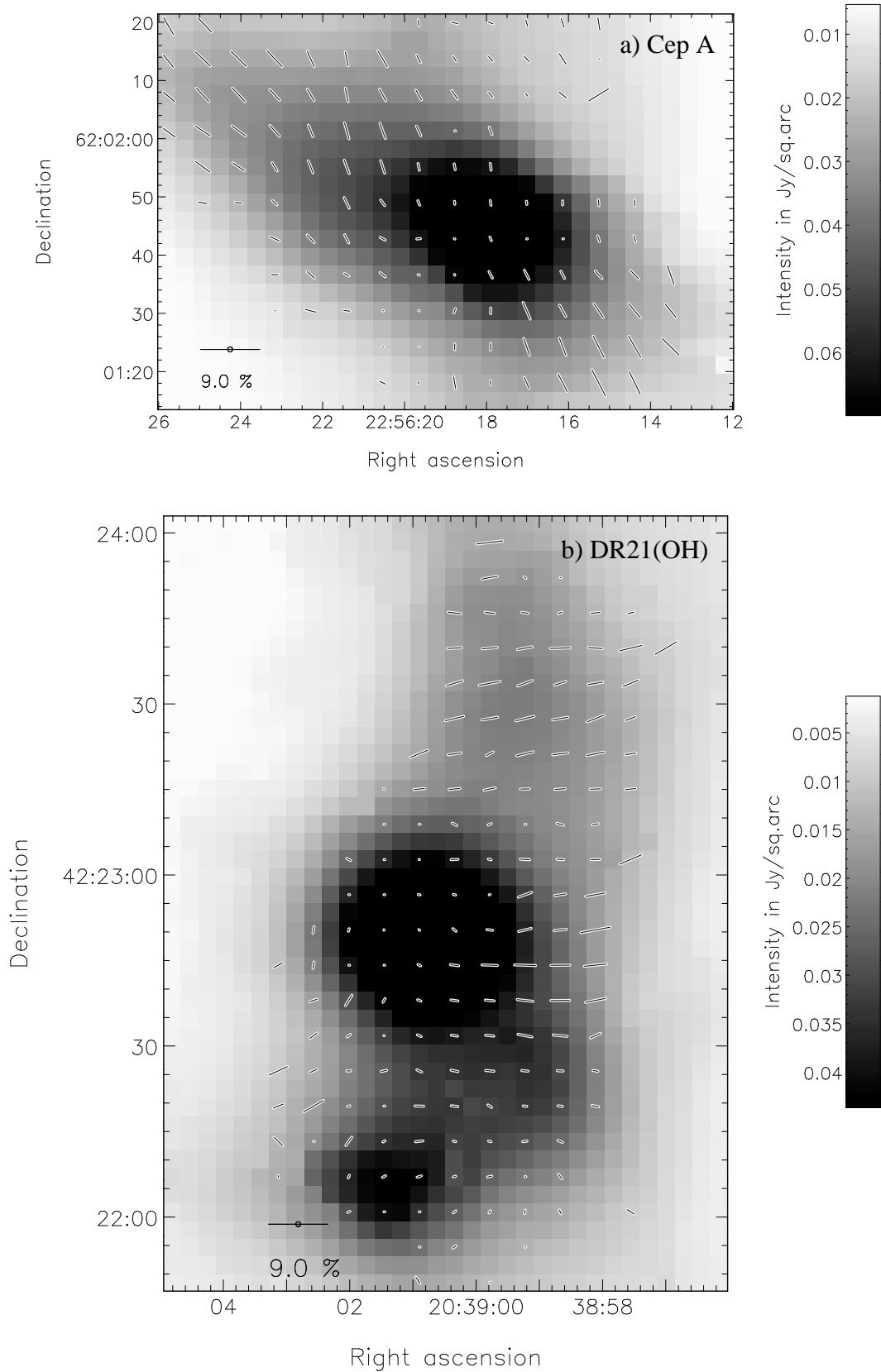


**Figure 1.** Final result of the data reduction method outlined in section 2. Epoch J2000. The greyscale is the total thermal continuum emission at 850  $\mu\text{m}$ , with the  $\mathbf{B}$ -vectors overlaid to represent the plane of the sky magnetic field direction. The polarisation percentage scale is presented in the lower left of each image, with the total intensity scale to the right of each image.

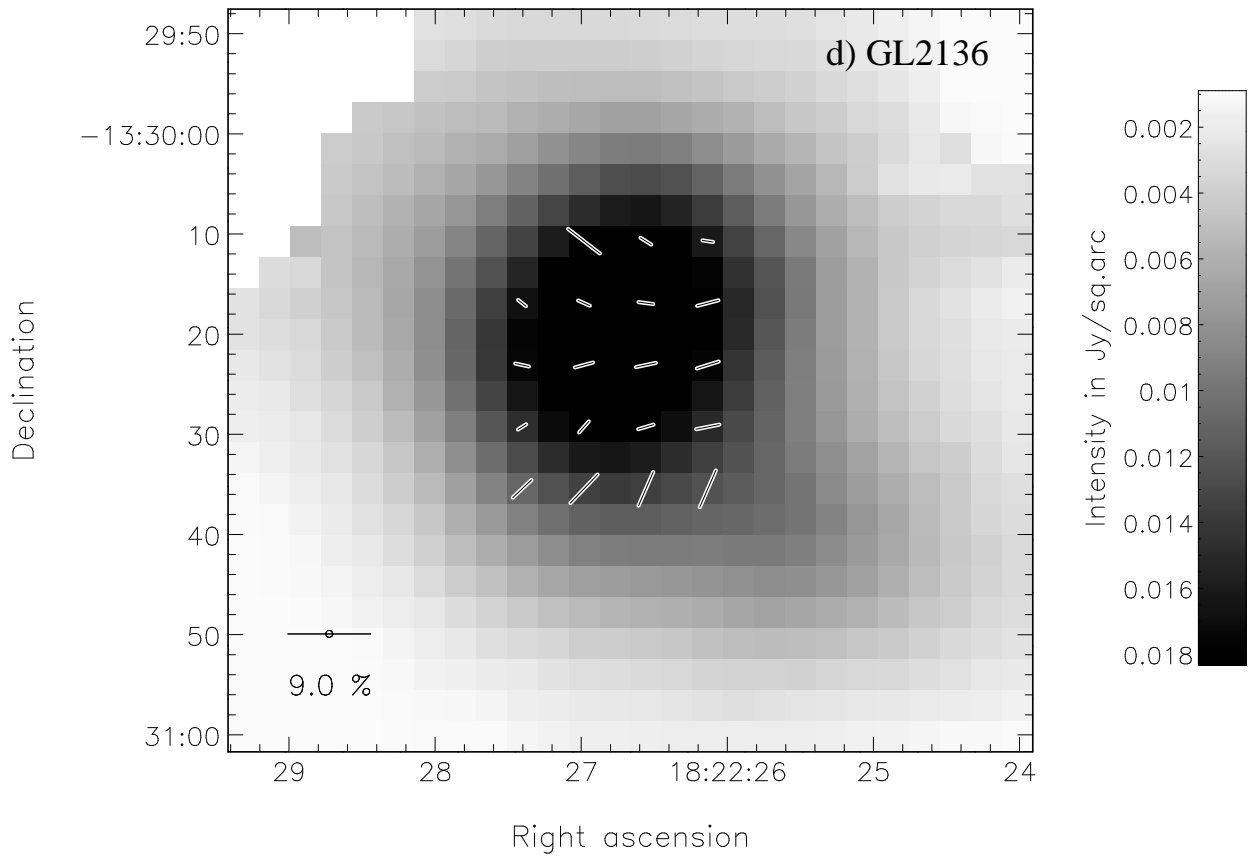
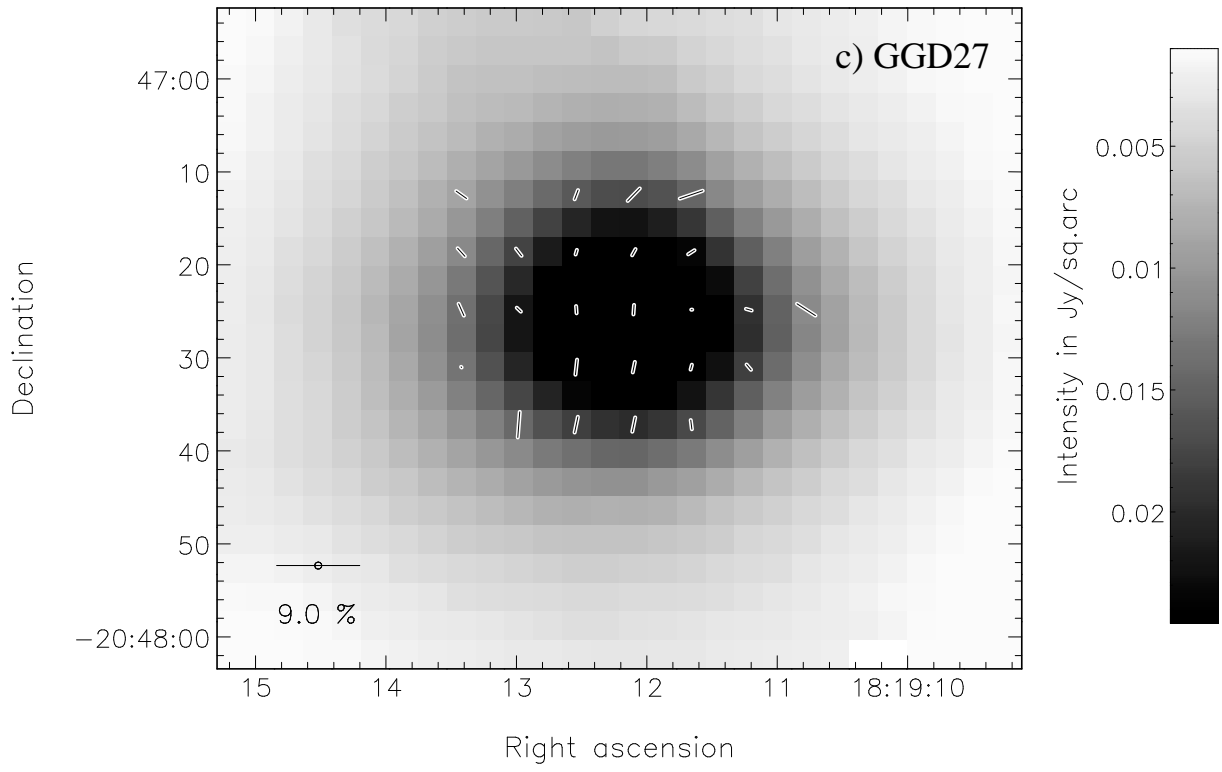


Figure 1 (continued)

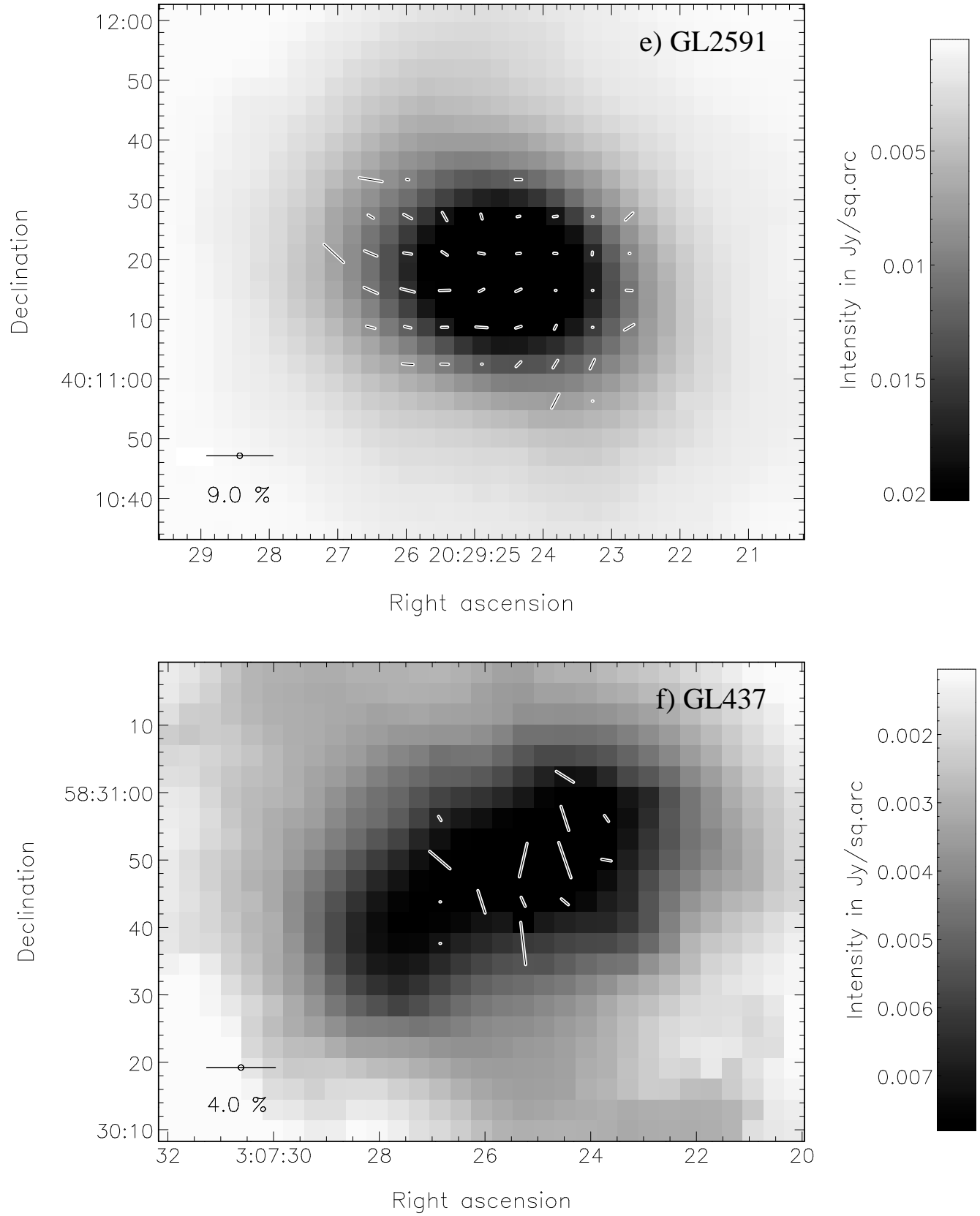


Figure 1 (continued)

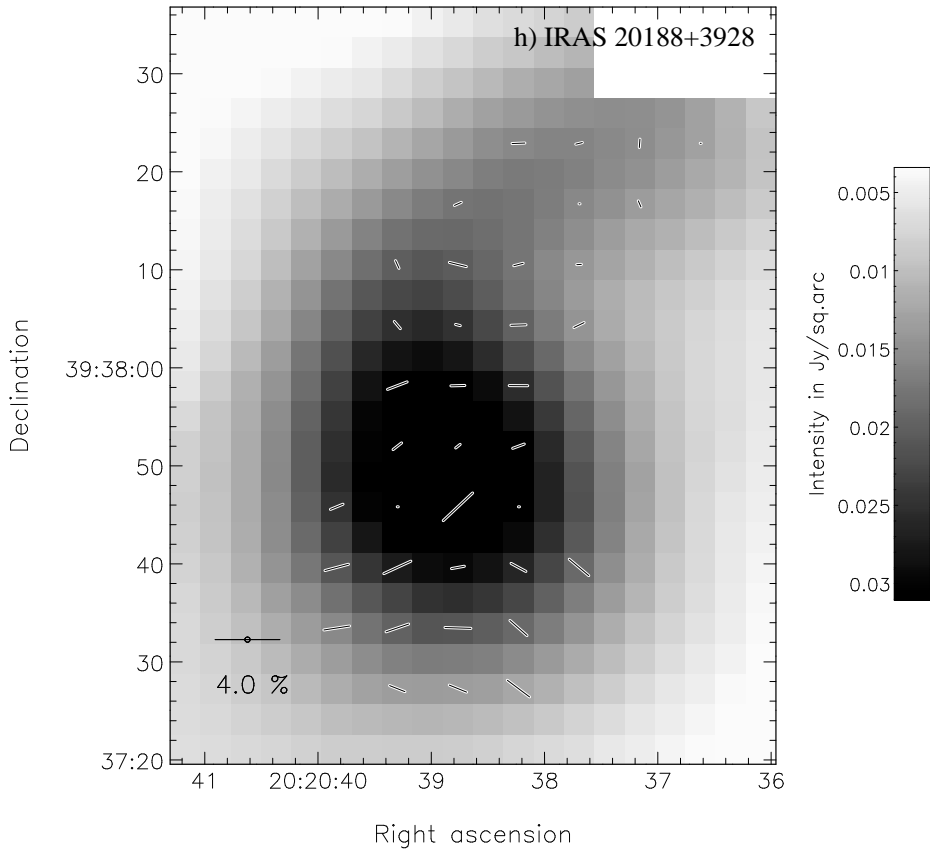
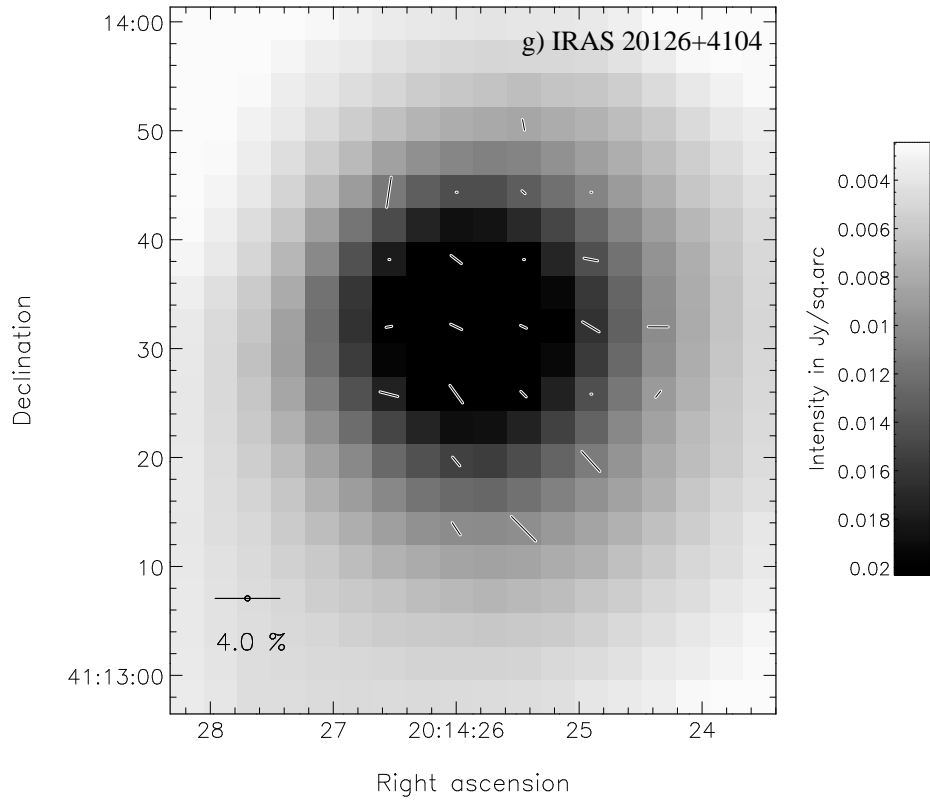


Figure 1 (continued)

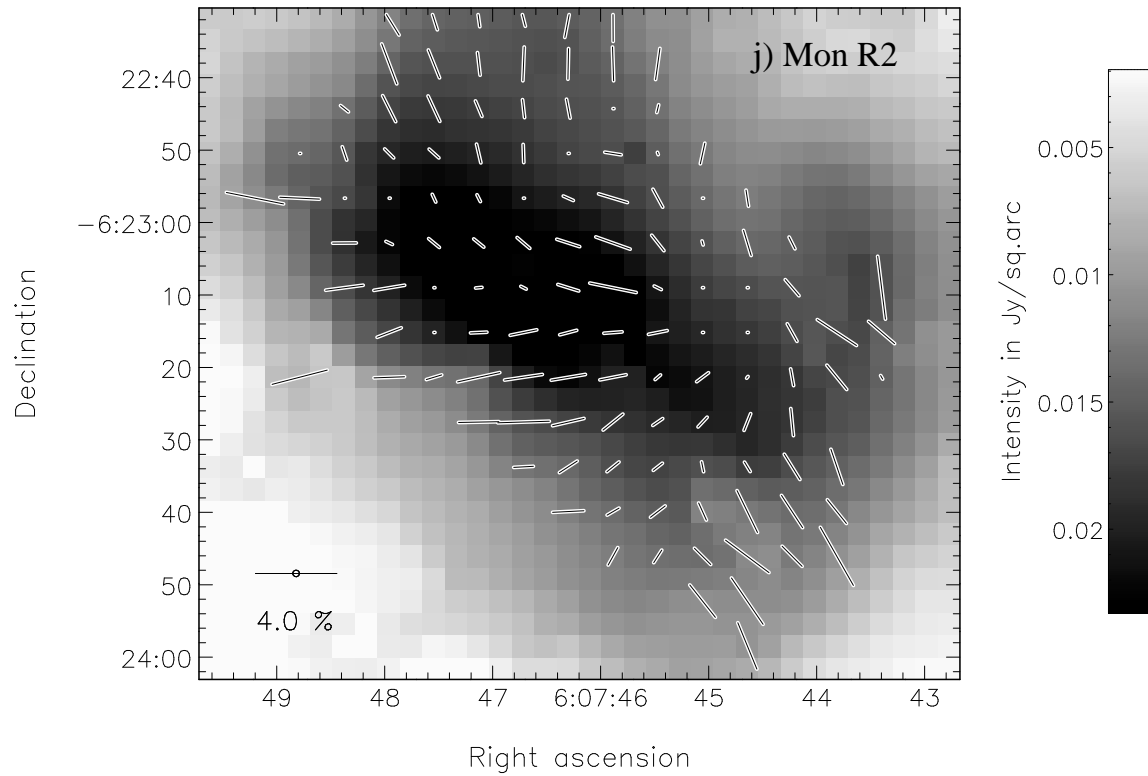
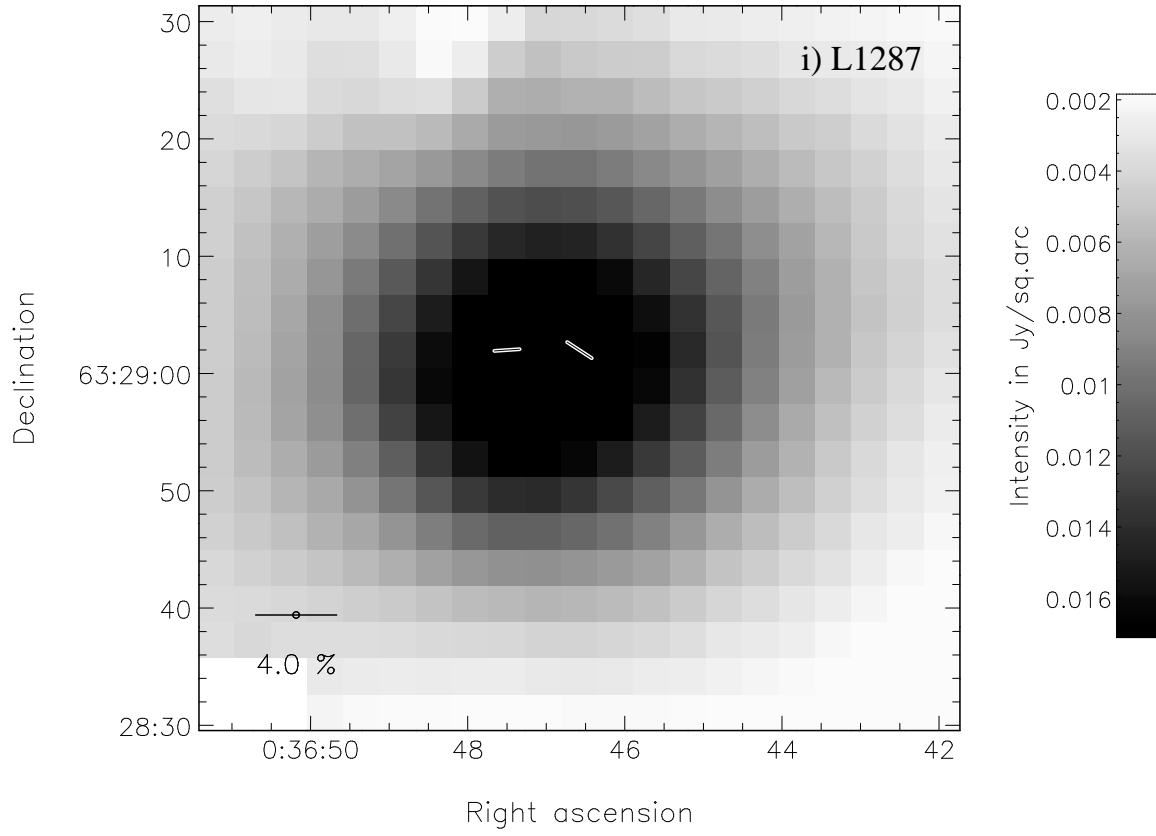


Figure 1 (continued)



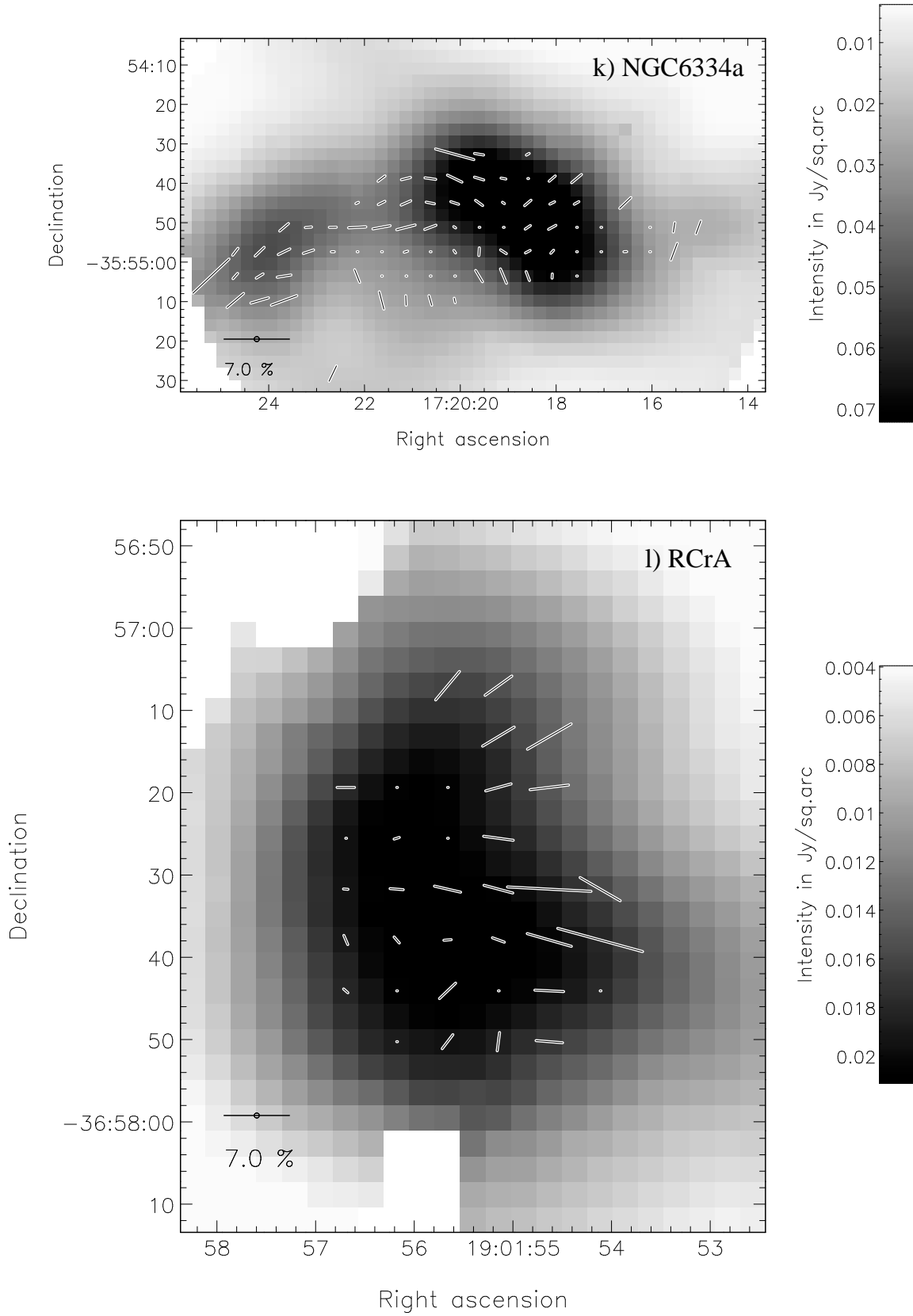


Figure 1 (continued)

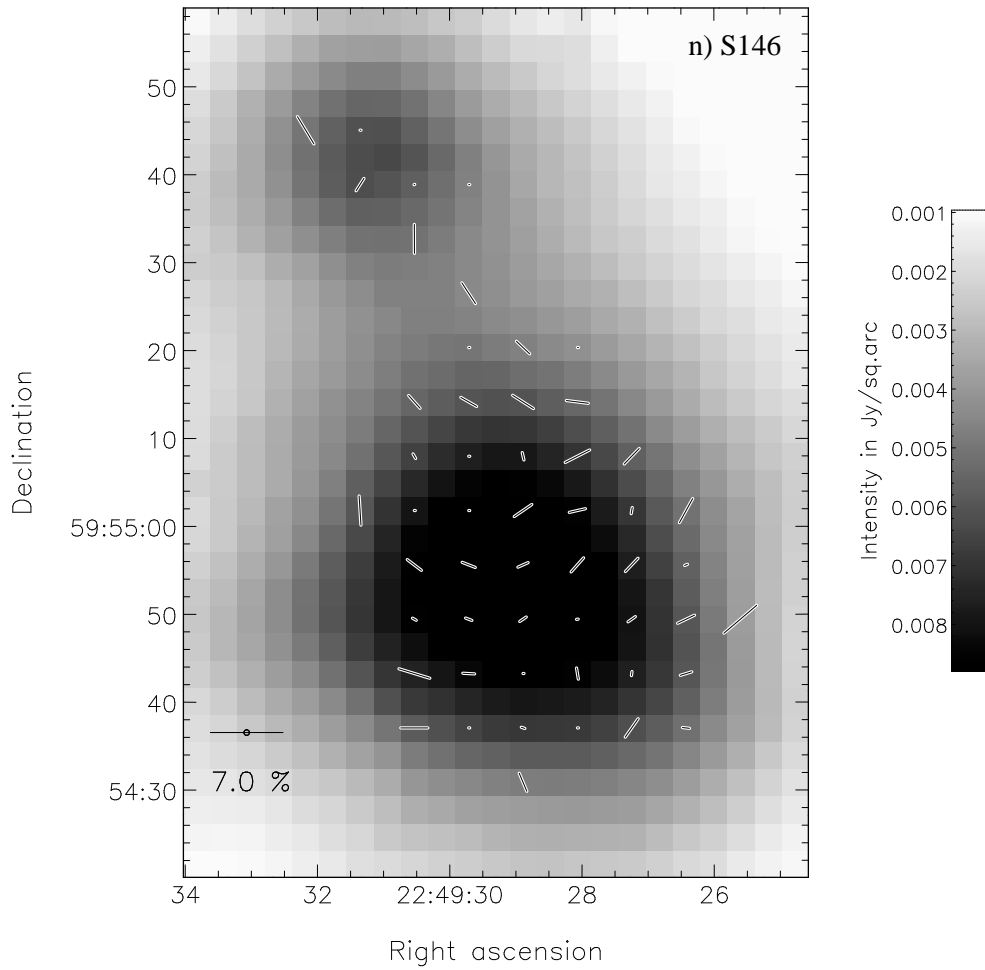
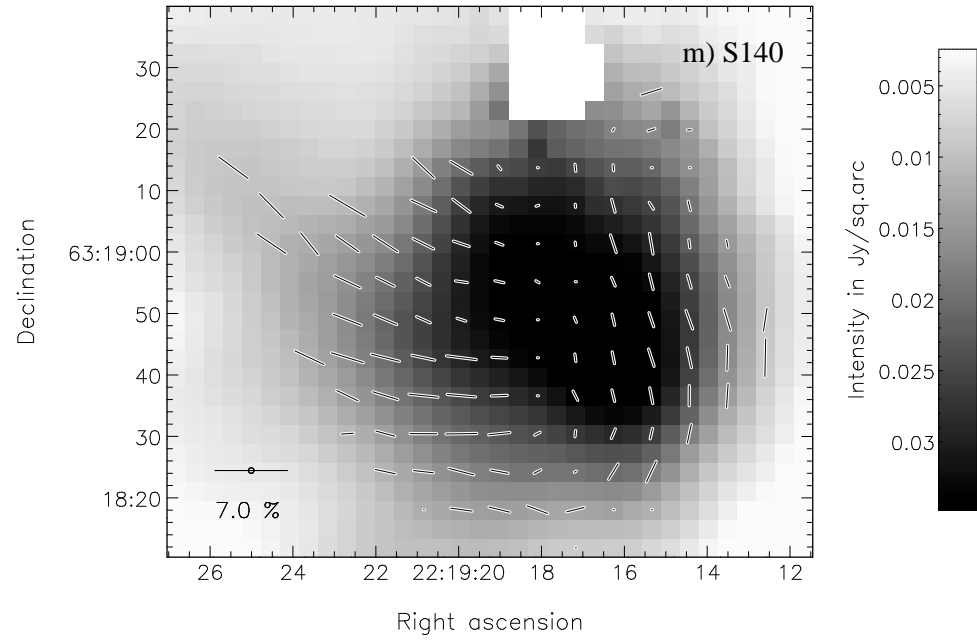


Figure 1 (continued)

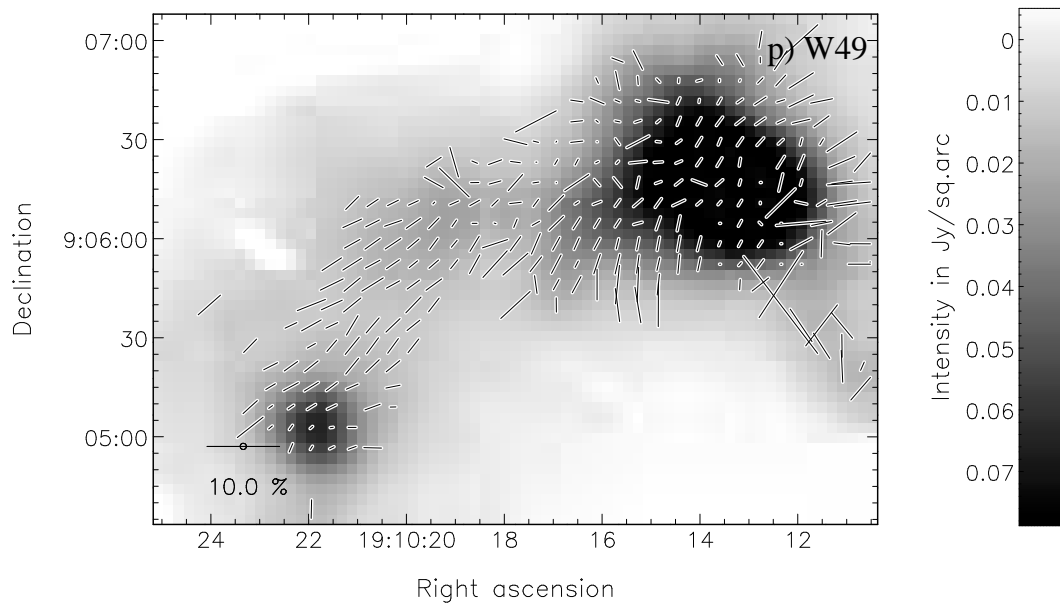
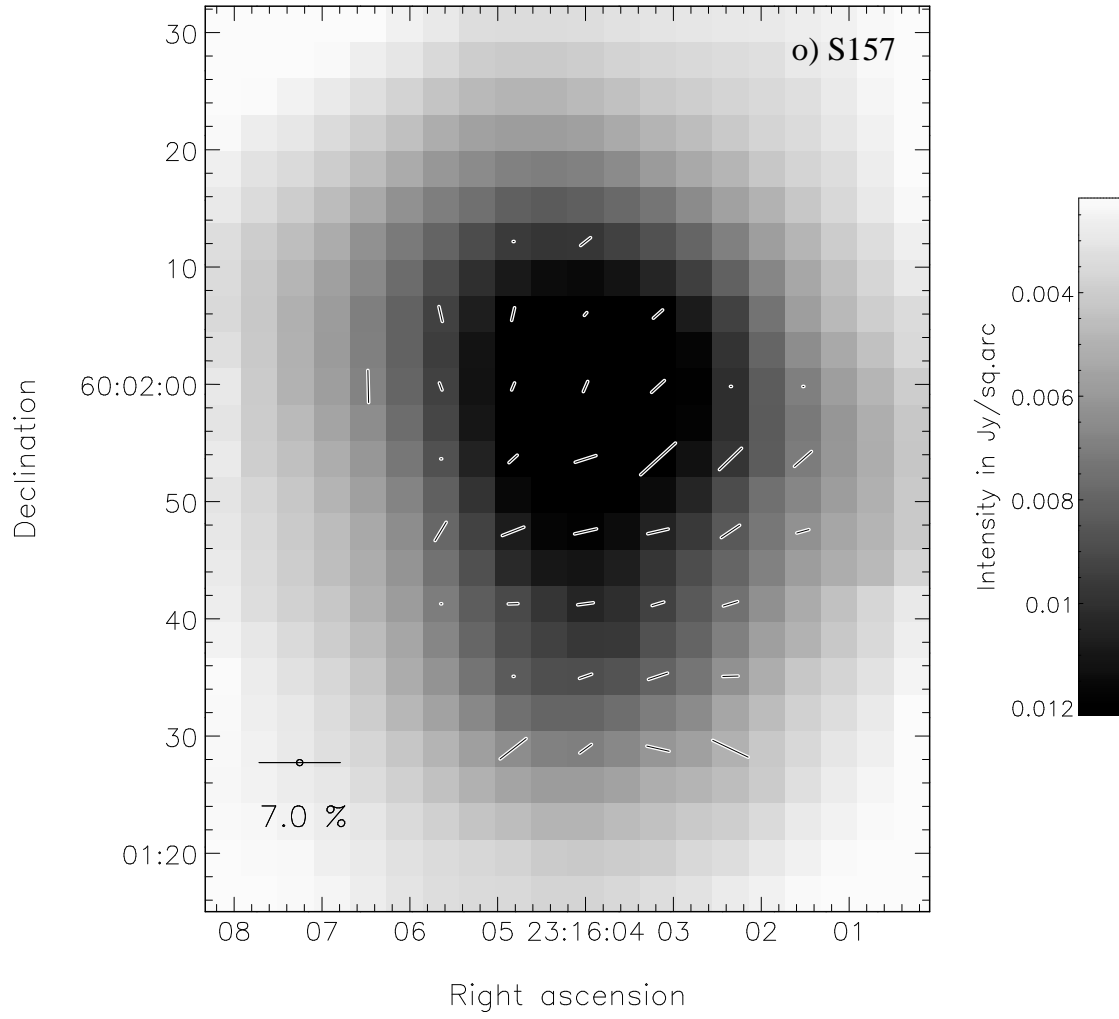


Figure 1 (continued)

**Table 2.** The sources with their observed parameters. Magnetic field strengths are not calculated for all cores, e.g. DR21(OH) Main. The vectors across the cores which have no field strength estimates have low polarisation signal-to-noise (see section 3.2).

Core	RA (hh:mm:ss)	DEC (° ' ")	Distance (kpc)	Temp K	Flux (850 $\mu$ m) (Jy)	Mass ( $M_{\odot}$ )	$n$ cm $^{-3}$	B mG	Temp. Ref. <sup>a</sup>
Cepheus A	22 56 17.9	62 01 49	0.725	35	117	200	$7.9 \times 10^5$	5.7	1
DR21(OH)N	20 38 59.5	42 23 31	3	20	41 <sup>b</sup>	2500	$1.6 \times 10^5$	1.1	2
DR21(OH) Main	20 39 00.8	42 44 49	3	58/30	60 <sup>c</sup>	900/2100	$1.8/4 \times 10^5$		2
GGD27	18 19 12.1	-20 47 31	1.7	20	34	660	$2.1 \times 10^5$	0.2	
GL2136	18 22 29.1	-13 29 46	2	28	28	470	$9.1 \times 10^4$	0.3	3
GL2591	20 29 24.9	40 11 21	1.5	28	34	320	$1.5 \times 10^5$	0.5	3
GL437	03 07 23.7	58 30 50	2	20	15	400	$7.8 \times 10^4$		
IRAS 20126+4104	20 14 26	41 14 42	1.7	27	26	330	$1.1 \times 10^5$	0.1	3
IRAS 20188+3928	20 20 39.3	39 37 52	4	39	48	2100	$5.1 \times 10^4$	0.2	4
L1287	00 36 47.5	63 29 02	0.85	34	24	60	$1.4 \times 10^5$		5
MonR2	06 07 46.3	-06 23 09	0.95	50	52	100	$1.7 \times 10^5$	0.2	6
NGC6334A	17 20 18.6	-35 54 45	1.7	50	149	870	$2.8 \times 10^5$	0.9	7
NGC6334AE	17 20 23.9	-35 54 55	1.7	50	75	440	$1.4 \times 10^5$		7
RCrA	19 01 53.6	-36 57 07	0.129	20	44	5	$3.6 \times 10^6$	1	
S140	22 19 18.1	63 18 49	0.9	27	72	260	$5.5 \times 10^5$	0.4	3
S146	22 49 29.1	59 54 53	4.7	42	17	1150	$1.3 \times 10^4$	0.1	8
S146N	22 49 30.9	59 55 30	4.7	20	5 <sup>c</sup>	900 <sup>c</sup>	$3.4 \times 10^4$		
S157	23 16 04	60 02 06	2.5	20	21	880	$8.8 \times 10^4$	0.2	
W49NW	19 10 13.2	09 06 14	11.4	45	288	86000	$9.1 \times 10^4$	<0.1	9
W49SE	19 10 21.8	09 05 03	11.4	45	61	18200	$1.9 \times 10^4$		9

<sup>a</sup> Where no reference is given, temperatures are assumed to be 20 K, consistent with the coldest measured temperature in this sample, DR21(OH). This therefore leads to upper limits for the masses of these objects.

<sup>b</sup> For a cylinder of radius 0.33pc (22.7'') and height 0.93 pc (64'').

<sup>c</sup> For a 40'' aperture, instead of a 60'', to stop contamination between sources.

Temperature references are: (1) Botinelli & Williams (2004); (2) Mangum, Wootten & Mundy (1992); (3) van der Tak et al. (2000); (4) McCutcheon et al. (1995); (5) Sandell & Weintraub (2001); (6) Thronson et al. (1980); (7) Sandell (1999); (8) Wu et al. (2005); (9) Harvey et al. (1977)

1992), d) extended shock-excited H<sub>2</sub> emission at 2.12 $\mu$ m (Bally & Lane 1982; Doyon & Nadeau 1988) and e) highly blueshifted Herbig-Haro objects with large proper motions pointing away from the activity centre (Lenzen, Hodapp & Solf 1984; Hartigan & Lada 1985; Hartigan et al. 1986; Lenzen 1988). The well known outflow in this region has a complex morphology. On scales of  $\sim 1$  pc, the outflow is in the east-west direction, but on smaller scales, there is an ionised jet that is oriented northeast-southwest. Narayanan & Walker (1996) argue that this may be due to multiple outflow episodes. They hypothesise that the older ( $3\text{--}20 \times 10^4$ yr) high-velocity outflow is oriented along the east-west direction, while the extremely high velocity lobes of the current flow ( $\leq 5 \times 10^3$  yr) extend to the northeast and southwest. On even smaller scales, there is evidence for a thermal radio jet with position angle  $\sim 48^\circ$ , which is perpendicular to a band of water maser positions that are thought to trace a circumstellar disc (Gómez et al. 1999).

The magnetic field in Cepheus A has been studied recently using Zeeman effect of H<sub>2</sub>O masers (Vlemmings et al. 2006) and OH masers (Bartkiewicz et al. 2005). Vlemmings et al. (2006) find that the maser emission associated with the HW2 high-mass young stellar object in this region, which is argued to trace the circumstellar disc, has a field strength of 100–600 mG. They find other masers further from HW2 to have magnetic field strengths of 30–100 mG. In all cases the magnetic field pressure is calculated to be similar to the dynamic pressure, indicating

the magnetic field is strong enough to control the outflow dynamics of HW2. Bartkiewicz et al. (2005) find that the magnetic field is extremely ordered on arcsecond scales, pointed away from us in the east, and toward us in the west. Their linear polarisation measurements from these masers reveal that the direction of the magnetic field in the plane of the sky is  $\sim 53^\circ$ , or roughly parallel to the radio jet axis.

The SCUBA polarimetry of Cepheus A (Fig 1a) reveal magnetic field vectors that are ordered around a position angle of  $50^\circ$  in the northeast of the observed region, and ordered  $\sim 40^\circ$  in the southwest of the region. There is a band of depolarisation across the core which has a position angle of  $\sim 135^\circ$  perpendicular to the inferred magnetic field direction. This plane of the sky magnetic field morphology is roughly parallel to the outflow/radio jet axis that has been observed on similar/smaller scales. This pattern of magnetic field vectors may be interpreted as a ‘pinched-in’ or hour-glass morphology, with the field twisted towards the centre of the source, where the depolarisation occurs.

CF calculations for the plane of the sky magnetic field strength lead to estimates of  $\sim 6$  mG. This is the strongest magnetic field calculated for the cores in this sample, but is smaller than the field strengths calculated from the maser emission (Vlemmings et al. 2006). This suggests that the magnetic field is weaker on larger scales, becoming stronger on smaller scales, closer in to the protostar. The data presented here, in conjunction with the findings of Bartkiewicz et al. (2005) and Vlemmings et al. (2006), lead

to a magnetic field that, in the plane of the sky, is northeast-southwest in direction, with the magnetic field in the northeast pointing away from us, and in the southwest pointing toward us.

## 4.2 DR21(OH)

DR21(OH) is part of the star forming complex W75, located in the Cygnus X region, at a distance of  $\sim 3$  kpc (Campbell et al. 1982). Its relative close proximity has aided in the fact that it is one of the most studied star forming regions in the Galaxy. The DR21 H II region is  $\sim 3'$  to the south of DR21(OH) and contains a cluster of late type O stars, and one of the most intense outflows known. DR21(OH) – also known as W75S or W75S(OH) – unlike DR21, consists of young stars in the process of forming, and as such offers a glimpse of an earlier stage of evolution of star formation. Previous continuum studies have shown that DR21(OH) is made up of three compact continuum sources, DR21(OH) Main, DR21(OH)S and DR21(OH)W, all of which seem to be actively forming stars (Mangum, Wootten & Mundy 1991). Higher resolution studies confirmed that DR21(OH)Main is in fact composed of two smaller cores, MM1 and MM2 (Woody et al. 1989).

The magnetic field of DR21(OH) is reasonably well studied, and there are Zeeman estimates of the line of sight magnetic field strength for MM1 and MM2 (Crutcher et al. 1999). Lai et al. (2003b) used BIMA to gain information on the magnetic field via polarimetry of both dust and CO, in order to map the magnetic field morphology in the plane of the sky. Comparisons of ion/neutral linewidths have also been used to establish a three-dimensional impression of the magnetic field (Lai et al. 2003a). The morphology of the field at the resolution sampled by BIMA indicates that the magnetic field is ordered, thus implying a strong field. The magnetic field is estimated to have a strength of  $\sim 0.4$  mG with an inclination of  $36^\circ$  to the line of sight, and a position angle of  $105^\circ$  in the plane of the sky (Lai et al. 2003a). The BIMA data only measure the polarised dust emission in patches, and do not reveal the magnetic field morphology throughout the whole region.

The data presented here (Fig 1b) include our observed data as well as some archival data for DR21(OH), which were observed on 2002 October 2 (Vallée & Fiege 2006), which effectively doubles the time on source for this target. The archival data were subjected to our method of data reduction as detailed earlier. The data reveal that the DR21(OH) region is composed (at this resolution) of one main core DR21(OH) Main. There are also two fainter cores close to the main core, one to the south-west, DR21(OH)W and one due south, DR21(OH)S. Mangum, Wootten & Mundy (1992) identified another core, DR21(OH)N, in  $\text{NH}_3$  emission, although in the SCUBA data presented here it appears to have the morphology of a ridge extending northwards from the main core. There are also molecular outflows associated with the main core emanating in an east-west direction (Lai et al. 2003b).

Our calculated mass of the Main core is somewhat larger than those of Mangum, Wootten & Mundy (1991), but they calculated the individual masses of MM1 and MM2 using OVRO interferometer measurements of the dust emission. It

is to be expected that our calculations reveal higher masses, given that they are based on single dish measurements and so include more diffuse dust on larger scales. Comparisons of our derived total masses with those of Vallée & Fiege (2006) reveal our masses are much higher than their estimates, however they have assumed a temperature of 100 K for both the Main and northern source. We also use larger apertures for our calculations. Once these two factors have been taken into account, the mass estimates are consistent.

The polarimetry indicates that the magnetic field is ordered across the ridge, parallel to the outflow axis. The percentage polarisation also remains stable (at  $\sim 3\%$ ) across the ridge. Across the main core the percentage polarisation drops, most apparently to the northeast of the core, coincident with MM1. This is observed in numerous other cores (for example, Chrysostomou et al. 2002; Matthews & Wilson 2002; Davis et al. 2000) and could be due to the magnetic field twisting within the JCMT beam, the grains becoming more spherical in regions of high density, or the grains being less efficiently aligned in regions of high density.

To the south of the main core, the vectors across DR21(OH)S are more dispersed in position angle, such that to the southwest of DR21(OH)S, the vectors have a position angle of  $\sim 135^\circ$ , changing to  $\sim 90^\circ$  northeast of the source. The vectors across the south-western core are  $\sim 90^\circ$ , the same as across the ridge.

The polarimetry data, in general agree with the findings of Vallée & Fiege (2006), however we see a smaller dispersion in position angles throughout the region, which may be due to a combination of higher signal-to-noise observations and a more careful data reduction. The polarimetry agree with the findings of Lai et al. (2003b), with the polarisation nulls coincident with MM1, where Lai et al. found very little polarisation from dust. The overall change in direction of the magnetic field across DR21(OH)Main also agrees with the BIMA data – both the dust and the CO polarimetry – indicating that the magnetic field stays ordered on both large and small scales. The observed polarisation nulls across MM1 may indicate that either MM1 has a twisted magnetic field in comparison to MM2, or that MM1 is more centrally condensed than MM2. Both of these would be consistent with MM1 being the more evolved of the two cores.

The polarimetry across the ridge (northern source) of the DR21(OH) region indicate an ordered field, which in itself implies a strong field. The field is (in the plane of the sky) perpendicular to the north-south ridge, yielding the possibility that collapse has occurred along the field lines. CF calculations reveal the magnetic field strength is of the order  $\sim 1$  mG in the plane of the sky. This is comparable to the field strengths previously calculated for the two sources in DR21(OH)Main by Crutcher et al. (1999) and Lai et al. (2003b), which were  $\sim 1$  mG in the plane of the sky from BIMA observations and  $\sim 0.5$  mG in the line of sight from Zeeman measurements. This indicates that the magnetic field is not only morphologically uniform throughout this cloud, but the strength is also reasonably uniform on different scales in the cloud. Vallée & Fiege (2006) estimated the strength of the magnetic field across the region as a whole (finding  $780\mu\text{G}$ ), across the main source (finding  $780\mu\text{G}$  again) and across the ridge to the north of the main core ( $\sim 200\mu\text{G}$ ). Our estimate of the magnetic field strength

across the ridge is consistent with their estimate across the entire region, but much greater than their estimate across the ridge, although they only use the four closest vectors to the source peak to calculate their field strengths, whereas we use all of the vectors which fall within the aperture used for the mass and density calculations.

#### 4.3 GGD27

GGD27 is located within Sagittarius, on the southwestern edge of a dark lane that runs in a northwest-southeast direction. Its kinematic distance has been calculated to be 1.7 kpc (Rodríguez et al. 1980) via the velocity of observed CO. It is a well known site of star formation, and located within the SCUBA submillimetre core (marginally resolved by the JCMT beam) are several infrared sources (Stecklum et al. 1997). There is a large-scale CO north-south outflow (blue lobe in the north) from an embedded source (IRS2) (Yamashita et al. 1987) as well as a CS disc elongated in the east-west direction. Martí, Rodríguez & Reipurth (1993) discovered one of the largest radio jets emanating from this region – its source being coincident with IRAS18162-2048, an extremely luminous star ( $2 \times 10^4 L_{\odot}$ ). They found the radio jet has a position angle of  $21^{\circ}$ , extends 5.3 pc, and is extremely collimated, with an opening angle of just  $1^{\circ}$ .

The polarimetry data of GGD27 (Fig 1c) imply a magnetic field that has a north-south direction, roughly parallel to the molecular outflow. To the north of the core, the polarimetry show that the magnetic field ‘fans out’ – the magnetic field vectors to the north-east of the core have a north-east orientation, whilst the vectors to the north-west of the core have a north-west orientation. This could be an indication that the field is pinched in closer to the core, although no depolarisation is observed across the core, suggesting that the magnetic field is not sufficiently twisted. The plane of sky magnetic field strength is estimated to be  $\sim 0.2$  mG.

#### 4.4 GL2136

Near-infrared studies of GL2136 (Minchin et al. 1991; Kastner, Weintraub & Aspin 1992) indicate that there is a circumstellar disc or torus roughly at a position angle of  $\sim 45^{\circ}$ . A kinematic distance of 2 kpc has been calculated by Menten & van der Tak (2004). Both water and OH maser emission has been observed, with analysis of the left and right circularly polarised components of the 1665 GHz feature leading to line of sight magnetic field estimates of 1 mG (Menten & van der Tak 2004). CO observations have revealed a massive ( $50 M_{\odot}$ ) molecular outflow from the source, perpendicular to the observed disc (Kastner et al. 1994).

The submillimetre continuum image of GL2136 (Fig 1d) reveals a marginally resolved object with a small extension to the southwest. The magnetic field vectors are mainly in the east-west direction, however in the south of the source they are more northwest-southeast orientated. The average position angle is  $102^{\circ}$ , around  $30^{\circ}$  away from the outflow direction. There is no depolarisation towards the centre of the core. CF calculations reveal plane of sky magnetic field strengths of  $\sim 0.3$  mG. This is less than half the value for

the line of sight component measured from maser emission, therefore, either the magnetic field is weaker on large scales, or, if we envisage the magnetic field wrapping around the outflow axis (which is close to the plane of the sky – see table 3), it must have a large toroidal component to produce the large line of sight component of the field strength – indeed, this may explain the relatively large ( $\sim 30^{\circ}$ ) difference between the outflow axis and the magnetic field direction.

#### 4.5 GL2591

GL2591 is a well-studied source, although its distance is still quite uncertain. Distance estimates range from 1 kpc (Mozurkewich, Schwartz & Smith 1986) to greater than 2 kpc (Merrill & Soifer 1974). The majority of estimates are between 1 and 2 kpc (e.g. Wendker & Baars 1974), therefore a mid-range distance of 1.5 kpc is adopted here. Hasegawa & Mitchell (1995) studied the molecular outflow in detail, finding a small-scale, well-collimated fast outflow in an east-west direction superposed on the previously known northeast-southwest, large-scale, less-collimated slow outflow.

Hutawarakorn & Cohen (2005) studied the magnetic field using Zeeman splitting of OH masers. The masers formed an elliptical shape perpendicular to the outflow axis, which was suggested to be a molecular torus of radius  $\sim 750$  AU, inclined at  $55^{\circ}$  to the line of sight. The magnetic field was found to range from -1.6 to +3.8 mG, reversing direction on opposite sides of the disc, indicating a toroidal component. The linear polarisation vectors were found to be both parallel and perpendicular to the outflow direction.

The SCUBA data (Fig. 1e) show a marginally resolved object, and the magnetic field vectors have, in general, an east-west direction across the core, parallel to the small-scale ( $90'' \times 20''$ ) outflow. The western side of the core has a polarisation null, and to the south of this, the magnetic field appears to be in a southeast-northwest direction. To the eastern side of the core, the vectors begin to curl up towards the northeast. The average position angle of the polarisation vectors is  $95^{\circ}$  aligning with the outflow axis. The polarisation null to the west of the object suggests a twisted field, agreeing with the findings of Hutawarakorn & Cohen (2005). The plane of sky field strength is estimated to be  $\sim 0.5$  mG. When compared with the estimates of Hutawarakorn & Cohen (2005), which indicate a strong toroidal field in the disc, the data imply that the magnetic field, once again, becomes weaker on larger scales.

#### 4.6 GL437

GL437 is located at a distance of  $\sim 2$  kpc (Arquilla & Goldsmith 1984). It is composed of a compact cluster of young stars (including B stars), and a reflection nebulosity which is centered on WK34 (Weintraub & Kastner 1996). There is also a broad molecular bipolar outflow that extends  $\sim 1$  pc and is orientated roughly north-south (Gómez et al. 1992), with the south lobe being blueshifted. The SCUBA data (Fig. 1f) reveal that this source is an elongated core orientated in the northwest-southeast direction. The polarimetry is aligned

such that the magnetic field appears to be projected perpendicular to the ridge of gas and dust forming the elongated source, roughly parallel to the outflow axis. There is a polarisation null to the southeast of the core, and the polarisation percentage changes seemingly randomly across the core.

#### 4.7 IRAS 20126+4104

IRAS 20126+4104 is located in the Cygnus-X region, at a distance of 1.7 kpc (Wilking et al. 1989). It is classified as a high mass protostellar object (HMPO; Sridharan et al. 2002) — although at a later stage of evolution than those discussed in Curran et al. (2004) — it is the high mass equivalent of a class 0/I protostar. It has a well known molecular outflow and an ionised jet. The CO outflow is roughly north-south in orientation (position angle of  $171^\circ$ ) with redshifted gas in the south and blueshifted gas in the north. The jet, detected by emission knots of H<sub>2</sub> and [SiII] has a position angle of  $117^\circ$  (Shepherd et al. 2000). Shepherd et al. (2000) conclude that the most likely interpretation for this is for the collimated jet to be precessing through an angle of  $\sim 45^\circ$ . More recently, Lebron et al. (2006) studied the kinematics of this region and concluded that whilst a precessing jet is supported by the data, multiple flows driven by independent sources cannot be ruled out.

The polarimetry data (Fig. 1g) reveal that the projected magnetic field has, in general a northeast-southwest orientation. This is roughly at an angle of  $\sim 40^\circ$  to the ionised jet, and almost perpendicular to the CO outflow, which may be evidence of a helical field. There are several polarisation nulls to the north of the core, away from the intensity peak. The plane of sky component of the magnetic field is small — only 0.1 mG.

#### 4.8 IRAS 20188+3928

IRAS 20188+3928 is located in the Cygnus region at an uncertain distance between 0.4–4 kpc (Little et al. 1988). All further calculations in this paper assume a maximum distance of 4 kpc, and so all values quoted are upper limits. Little et al. (1988) observed this region in CO and HCO<sup>+</sup>, and found a CO bipolar outflow, which has a north-southwest direction. The redshifted gas is to the north, and the blueshifted gas is in the southwest. The SCUBA data (Fig. 1h) shows a curved ridge of gas and dust extending from the north of the core, curling around to the west. The polarimetry (in general) indicate that the magnetic field lines are east-west in orientation, projected onto the plane of the sky. Towards the southwest of the core, the polarimetry vectors begin to deviate from the east-west orientation towards a northeast-southwest orientation, aligning with the outflow in the southwest. The degree of polarisation is measured to be (on average) lower across the ridge than across the brighter core. A plane of sky field strength component of  $\sim 0.2$  mG has been calculated.

#### 4.9 L1287

L1287 is a dark cloud at a distance of 850 pc (Yang et al. 1991). There is an energetic outflow associated with the

cloud, orientated in a northeast-southwest direction. At the centre of the outflow there is a very cold IRAS source IRAS 00338+6312 (Yang et al. 1991). The submillimetre data (Fig. 1i) reveal a marginally resolved object. There is little polarimetry (2 vectors) as the integration time for this object was only 0.85 hrs, and so the errors in polarisation are large.

#### 4.10 MonR2

Monoceros R2 is a site of ongoing star formation, with a compact HII region (Wood & Churchwell 1989) and H<sub>2</sub>O and OH masers (Downes et al. 1975; Knapp & Brown 1976). The outflow in this region is one of the largest known, with a total extent of 6.8 pc (assuming a distance of 950 pc; Racine & van de Bergh 1970). This outflow extends to the north, east and south-west of the region. Giannakopoulou, Mitchell & Hasegawa (1997) assume that the large scale north-southwest outflow is old, and that the source of this outflow is now inactive, as the lobes are not well collimated. The easterly outflow is thought to be a relatively young, small-scale outflow, unresolved, from another source within the region. The polarimetry of this region (Fig. 1j) indicate that the magnetic field aligns with the outflows — the vectors are oriented north-south in the north of the region, east-west in the east of the region and northeast-southwest in the southwest of the region. The morphology of the magnetic field is complex, with a plane of sky magnetic field strength of  $\sim 0.2$  mG.

#### 4.11 NGC6334A

NGC6334A is a giant HII region/molecular cloud complex and is located close to the galactic plane at a distance of 1.7 kpc (Neckel 1978). NGC6334-submm has two cores, one in the east, and a brighter core (probably multiple, but not resolved within the JCMT beam) in the west of the image. There is a CO bipolar outflow associated with NGC6334A, which lies almost in the plane of the sky (Sarma et al. 2000) in a north-south direction (De Pree et al. 1995). There is a ridge of material between the two cores in which the polarimetry (fig. 1k) suggests that the magnetic field is parallel to the ridge. The magnetic field across the faint core has a southeast-northwest direction, which curls round to east-west across the ridge. The magnetic field across the brighter main core is more complex, in the northeast of the core, the magnetic field has a northeast-southwest direction, but towards the southwest of the core, it is directed northwest-southeast, and in the very southwest of the region there is a polarisation null. The abrupt change in the orientation of the magnetic field may be due to two cores being present, although unresolved in the JCMT beam. Previous observations of OH maser emission have yielded estimates of the line of sight magnetic field strength of  $\sim 0.35$  mG toward the source, with maximum strengths of 0.5 mG (Mayo et al. 2004). The polarimetry presented here lead to estimates of the plane of the sky component of the field strength to be  $\sim 0.9$  mG, consistent with the previous line of sight measurements.

#### 4.12 RCrA

The molecular complex Coronae Australis is  $\sim 129$  pc away from the Sun (Marraco & Rydgren 1981), and is dominated by the centrally condensed core centred near the emission line star R Cr A. Nutter, Ward-Thompson & André (2006) have recently studied this source in the submillimetre, and reveal three submillimetre peaks within the main source, named SMM-1A,B and C. SMM-1A is located in the south-eastern part on the core, with SMM-1B and C being located in the north-east and northwest of the core.

R Cr A is one of the more evolved sources in the polarimetry sample, and is classified as a Herbig Ae star (Marraco & Rydgren 1981). There is a CO bipolar outflow with a position angle of  $\sim 90^\circ$  in the region of R CrA (Walker, Lada & Hartigan 1985) but more recent molecular line mapping by Anderson et al. (1997) has cast doubt on whether R CrA is the driving source. The polarimetry of the R CrA region (fig. 1l) indicate that the magnetic field is roughly parallel to the direction of the outflow (see also Clark et al 2000). There are also polarisation nulls across this source, in two regions — one in the north of the source, and one in the south. A plane of sky field component of 1 mG has been calculated.

#### 4.13 S140

S140 is located in the Cepheus ring, at a distance of 900 pc (Preibisch & Smith 2002). S140 has two outflows, one with a position angle of  $\sim 160^\circ$ , which is bipolar in nature, and another smaller scale outflow which has a position angle of  $\sim 20^\circ$  (Preibisch & Smith 2002). The higher resolution K'-band data of Weigelt et al (2002) show arc-like structures protruding from the northeast of the source which are proposed to trace outflow cavities carved out by material flowing away from S140 IRS1. The resolution of their data is 240 milli-arcsec and covers an area of  $13'' \times 21''$  — approximately one beam width of the SCUBA data presented here. The SCUBA data (fig. 1m) show that the magnetic field vectors are ordered, in a north-south direction to the western side of the source, whereas in the east, the magnetic field is east-west orientated. OH Zeeman observations (Baudry et al. 1997) have revealed line of sight field estimates of +2.8 mG. CF estimates of the plane of sky component of the field lead to strengths of  $\sim 0.4$  mG, which either indicates the magnetic field is mainly in the line of sight, or, that the field is stronger on smaller scales. There is a faint ridge of gas and dust extending from the east of the source, curling northwards, which the magnetic field vectors seem to follow, running parallel to it (in the plane of the sky). It may be possible that the arc-like structure in the SCUBA image is related in some way to the smaller scale outflow cavities seen by Weigelt et al (2002).

#### 4.14 S146

S146 is located at a distance of 5.2 kpc (Wu et al. 2005). A bipolar molecular outflow, in a north-south direction (north lobe blueshifted), driven by a star of spectral type O6.5 or earlier (required to account for the ionisation of the HII region). In the submillimetre data (fig. 1n) there are two cores in a north-south configuration. There is a ridge of gas and

dust seemingly connecting the two cores. The polarimetry appears to be almost randomly distributed, with several polarisation nulls on the northern core, and to the north and south of the southern core, although there does not seem to be a relation between the intensity and polarisation percentage. The large scatter of the polarimetry vector position angles may suggest that the magnetic field is weak across this region. It may also be explained if the magnetic field was predominantly in the line of sight (the outflow is mainly in the line of sight — see table 3), which can cause random polarisation patterns and/or low polarisation percentages. The plane of sky component of the field strength is calculated to be 0.1 mG, which is one of the weakest measured for this sample.

#### 4.15 S157

S157 is a diffuse nebula located towards the Cassiopeia-Perseus arm at a distance of  $\sim 2.5$  kpc, and is surrounded by HII regions and young open clusters (Shirley et al. 2003). The submillimetre data (fig. 1o) show the region is only slightly more extended than a point source, with bright submillimetre emission extending southwards from the main core. The polarimetry of the core show that the magnetic field vectors have an east-west direction to the south of the core, but in the north, the vectors are aligned roughly northwest-southeast. There are two regions of null polarisation — one in the northwest of the source, the other in the southeast. The plane of sky field strength component is estimated to be  $\sim 0.2$  mG.

#### 4.16 W49

W49 is in the galactic plane at a distance of 11.4 kpc (Gwinn, Moran & Reid 1992), and is one of the most luminous HII regions in the Galaxy Smith et al. ( $\sim 10^7$ , 1978). There are two bright cores in this region (fig. 1p) — one in the northwest, W49N, and one in the southeast, W49SE, with a third fainter source along the ridge in between the brighter two cores, W49E. This ridge differs from those previously mentioned, as it is much more extended and less concentrated (fainter). There is a CO bipolar outflow from W49N, with the redshifted lobe to the north and blueshifted to the south. The outflow is almost in the line of sight (Scoville et al. 1986). The polarimetry vectors are aligned such that the magnetic field lines run from one core to the other, parallel to the ridge. Across the W49N core, the magnetic field (plane of the sky component) is estimated to be less than 0.1 mG. The outflow is in the line of sight, however, and so this may suggest that there is a larger line of sight component to the magnetic field.

## 5 DISCUSSION

### 5.1 Comparison of Outflow & B-field directions

Theoretically, magnetic fields play an important role in the launching and collimation mechanisms of outflows, and so it would be of interest to see if any relationship between the observed magnetic field direction on these large scales, and the jet/outflow axis exists. Previous studies of the



**Table 3.** Outflow and magnetic field alignment. The columns are (1) the region name, (2) the variance in polarisation percentage, (3) the average polarisation percentage measured across the region, (4) the mean position angle of the magnetic field vectors, (5) the outflow direction, (6) the difference between the mean position angle of the magnetic field vectors and the outflow, (7) the opening angle of the outflow, (8) the inclination (from the plane of the sky) of the outflow, (9) notes and reference.

(1) Region	(2) $\bar{P}$ %	(3) $\sigma_P^2$	(4) P.A. °	(5) Outflow P.A. °	(6) $ \delta\theta $ °	(7) Opening Angle	(8) Inclination	(9) Notes/References
Cepheus A	1.7	1.3	52	45	7	15-20°	pos (62°)	Patel et al. (2005)
				90	38	60°	pos (62°)	Patel et al. (2005)
DR21(OH)	1.3	1.0	98	90	8		pos	Lai et al. (2003b)
GGD27	1.2	0.5	105	20	85	1°	~pos	Gómez et al. (2003); Martí et al. (1999)
GL2136	2.3	1.3	102	135	33	60°	pos	Kastner et al. (1994)
GL2591	1.0	0.6	96	45	51	<90°	45°	Hutawarakorn & Cohen (2005)
				95	1	<90°	45°	more collimated than the 45° outflow
GL437	1.0	0.6	50	0	50	low	pos	Meakin, Hines & Thompson (2005)
IRAS 20126+4104	0.8	0.4	74	117	43	21°	pos	Hofner et al. (2007)
				171	83	70°	pos	Hofner et al. (2007)
IRAS 20188+3928	0.9	0.3	90	0	90		los	
				45	45		los	
L1287	1.4	0.02	75	45	30	50°	pos (60°)	Umemoto et al. (2000)
MonR2	1.2	0.7	64	0	64		los	Xu et al. (2006)
				45	19		pos	
				90	26		los	
NGC6334A	0.9	0.8	96	0	84		pos (10°)	Sarma et al. (2000)
RCrA	2.5	7.0	95	90	5	60°	pos	Anderson et al. (1997)
S140	1.5	1.0	70	20	50		pos	Preibisch & Smith (2002)
				160	90		los	Minchin, White, & Ward-Thompson (1995)
S146	1.3	1.1	86	0	86		los	Wu et al. (2005)
W49NW	2.2	3.2	119	0	61	30°	los	

alignment of T-Tauri stars with the local magnetic field (Ménard & Duchêne 2004) reveal a possible connection between the strength of the CTTS jets and their orientation with respect to the magnetic field. Interestingly, they conclude that the CTTS's with jets align to the magnetic field, but as a whole sample (i.e. both CTTS's with and without jets), the population is randomly orientated with respect to the magnetic field, which they say suggests either the influence of the magnetic field is dominant at large scales (whole cloud) but largely decreases on the much smaller scale of individual objects, or, the orientation of the CTTS's has changed since they first formed.

Table 3 shows the mean polarisation percentage, position angles of the magnetic field and outflow, and the difference between the magnetic field and outflow directions. The determined magnetic field vectors are not true (i.e. undirectional) vectors. They have a 180° ambiguity, and as such have position angles of between 0° and 180°. The magnetic field direction for each region is determined by calculating the weighted mean of the measured vectors. The smallest difference between the magnetic field direction and the outflow direction is assumed, and the results are plotted in fig. 2. Figure 2 is a cumulative distribution function, which shows that, for the whole sample (excluding S157, which as yet has no identified outflow, to the authors knowledge), given the (weighted) mean position angle of the magnetic field vectors, the magnetic fields within the sample appear randomly oriented with respect to the the jet/outflow direction. The Kolmogorov-Smirnov test reveals the whole sample has a 84.9% chance of being randomly orientated.

The sample has been split into two sub-samples – those

which have the outflow axis mainly in the plane of sky (i.e.  $i > 45^\circ$  to the line of sight), and those which have the outflow axis close to the line of sight ( $i < 45^\circ$ ). GL2591 is not included in either of these sub-samples however, as the outflow axis lies close to  $i \sim 45^\circ$ . Whilst all of the sources with very small differences are in the plane of sky subsample, the cumulative distribution function does not deviate significantly from a random distribution, and the Kolmogorov-Smirnov test leads to a 57.2% chance of random orientation. However, the line of sight sub-sample, with no sources showing good alignment between magnetic field and outflow axis, does deviate significantly from the random distribution (a 36.6% chance of random orientation from the Kolmogorov-Smirnov test), suggesting a relation between the misalignment of the (plane of the sky) field and outflow when the outflow lies close to the line of sight. If an alignment between the magnetic field and the outflow axis does exist and the outflow is close to the line of sight, it would be difficult to assign a direction to the magnetic field, and so misalignment between the inferred field and outflow direction is more likely.

Previous mid-infrared spectropolarimetry (Aitken et al. 1993) reveal that for their sample, overall, there is a large toroidal magnetic field component within the molecular structures associated with embedded young stellar objects. Their sample includes three sources from the sample in this paper – S140, MonR2 and GL2591. Their results for S140 and MonR2 agree with the findings of this paper – namely that there is a  $\sim 40^\circ$  difference in alignment. However, they find the magnetic field of GL2591 to be perpendicular to the  $90^\circ$  outflow, whereas we find it in almost perfect alignment.

This may be due to either a changing magnetic field morphology on different scales, or the magnetic field may have a stronger toroidal component closer in to the protostar/disc. Compared to the submillimetre, the mid-infrared emission comes from closer in towards the source, and it is higher resolution (has a smaller beamsize).

The alignment analysis carried out here needs to be treated with caution, for some regions, e. g. MonR2, S140, the mean position angle may not accurately represent the field direction. MonR2, as with some of the other sources, is an extended source, and the polarisation pattern indicates abrupt changes in the direction of the magnetic field. For sources such as these, the best alignment comparison may be made using modal position angle values (in sufficient bins), or possibly from the map itself.

Included in table 3, where possible, are the opening angles for the jets/outflows. Upon quick inspection, it is clear that, with the information present, there appears to be no relation between the degree of collimation and the alignment. GL2591 has a well collimated jet (position angle  $\sim 95^\circ$ ) which is almost perfectly aligned to the magnetic field, whereas RCrA has an opening angle of  $60^\circ$ , and again is well aligned to the magnetic field. GGD27 has a well collimated jet with an opening angle of only  $1^\circ$ , but the axis is almost perpendicular to the magnetic field. More information regarding the opening angles of such jets and outflows is needed to enable a more detailed analysis.

## 5.2 Field Morphology & Submillimetre Emission

A variety of continuum emission morphologies have been observed within this sample. Whilst the majority (11 out of 16) of the sources have a seemingly roughly spherical dense core (marginally resolved in the JCMT beam), several of these sources also exhibit more extended emission associated with the dense core (e. g. Cepheus A, DR21(OH), IRAS 20188+3928). Of these sources, the polarisation percentage often decreases with increasing intensity across the cores, whereas in the extended emission the polarisation percentage often remains stable. This may be due to the gas and dust being less dense in the regions of the extended emission, or may be the magnetic field has a simpler, less twisted morphology in these areas. Morphologically, field lines both parallel (Cepheus A, W49) and perpendicular (DR21(OH), S157) to the major axis of the extended emission are observed.

This sample also included dense cores which deviate significantly from spherical (at least in the plane of the sky, e.g. GL437, MonR2, NGC6334A). Of these sources the magnetic field is observed to be perpendicular to the major axis of the core in GL437 and RCrA. The field morphology of MonR2 and NGC6334A are complex, with the fields changing direction abruptly. This may be due to multiple cores unresolved by the JCMT beam.

## 5.3 Field Strength & Cloud Support

The plane of the sky magnetic field strengths have been calculated based on signal-to-noise (3) clipped vectors. The fields range from  $<0.1$  mG (W49N) to 5.7 mG (Cepheus A), although the majority of them are around 0.2–0.4 mG.

Out of the three strongest magnetic fields (Cepheus A, DR21(OH)N, RCrA), both DR21(OH)N and RCrA have field morphologies that may indicate ambipolar diffusion (the field is perpendicular to the major axis of the emission). Cepheus A, however, has the strongest field, and the field is parallel to the major axis of the extended emission. Previous polarimetric studies of W48 and S152 (Curran et al. 2004), reveal magnetic field strengths and polarisation patterns consistent with the findings in this paper. W48 exhibits depolarisation across the main core, whereas the polarisation percentage remains the same across the candidate HMPO W48W. S152 is a more complex region, consisting of ridges of gas and dust and the S152SE core – the candidate HMPO. The magnetic field is both parallel and perpendicular to the ridges in places, but across the S152SE core, the polarisation percentage remains at  $\sim 8\%$  and the field is perpendicular to the major axis of emission. The field strengths across the candidate HMPOs were calculated to be 0.7 mG for W48W and 0.2 mG for S152SE, consistent with the magnetic field strengths calculated for the star forming regions in this paper.

## 6 CONCLUSIONS

We present the largest (to date) sample of high mass star forming regions observed using submillimetre polarimetry. We describe an improved method of SCUBA polarimetry data reduction. The magnetic field geometries (from the intensity weighted vectors, projected onto the plane of the sky) are presented, along with calculations of the core masses, densities and field strengths.

The sources observed reveal a variety of morphologies for both the continuum emission and the magnetic field. The majority of the sources have dense cores that are unresolved in the beam, but some also have extended emission associated with the cores. In several of the regions, the polarimetry is uniform, suggesting ordered, relatively strong magnetic fields. A decrease in polarisation percentage across the cores is often seen, suggesting twisting or non-alignment of the dust grains in these cores. The polarisation percentage often remains stable across the extended emission, which may imply that in these areas, the magnetic field has a simpler, less twisted morphology, or it may be that as the extended emission is less dense, the dust grains do not become misaligned to the magnetic field. We see field morphologies perpendicular to the major axis of the continuum emission (DR21(OH), RCrA, S157), which could suggest ambipolar diffusion for these sources. It should also be noted that both of these regions which have outflows, have magnetic fields that align well with the outflow axes. We also see fields that are parallel to the extended emission, e.g. Cepheus A, however, the field in this region also aligns well with the outflow axis, and has the strongest magnetic field strength in this sample. It is interesting in this case that the extended emission is in the direction of the outflow.

An analysis of the mean position angle of the polarisation vectors and the outflow axes has been carried out. Whilst the sample as a whole has a cumulative distribution function similar to that expected if the magnetic field and outflow axes were randomly orientated, if the sample is broken down by inclination, into those predominantly in the line

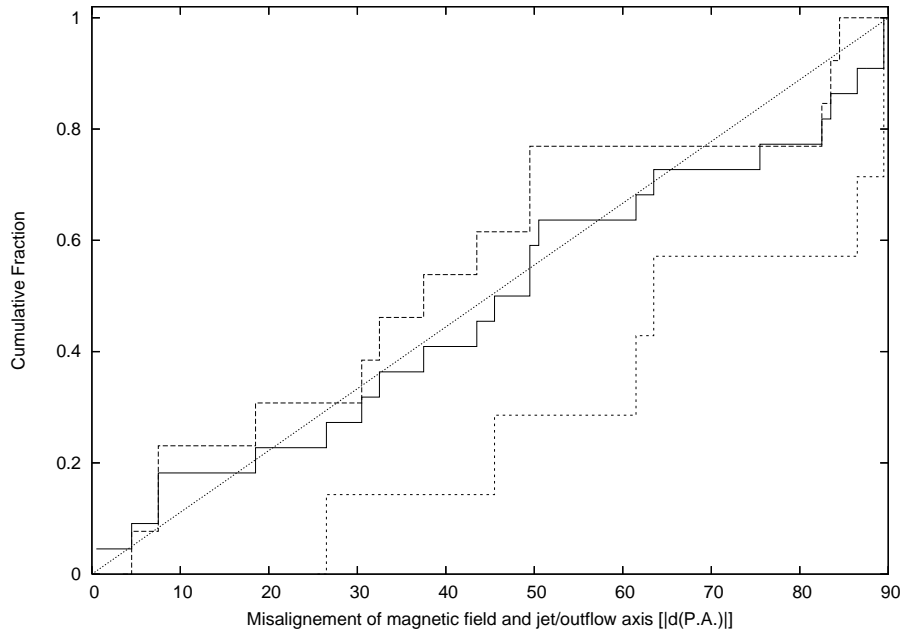


**Figure 2.** Cumulative distribution function of the difference in position angles between the weighted mean of the magnetic field vectors and the jet/outflow axis. The long dashed histogram is for all sources with outflow axes close to the plane of the sky ( $i > 45^\circ$ ), the small dashed histogram is for all sources with outflow axes close to the line of sight ( $i < 45^\circ$ ), the solid histogram is for the whole sample. The dotted line is the function expected for an infinite randomly oriented sample.

of sight, and those predominantly in the plane of the sky, the line of sight sample distinctly favours non-alignment, which would be expected if the magnetic field had a large line of sight component too, as it is then difficult to establish a magnetic field direction from the polarimetry. The plane of the sky sample only shows a marginal increase in alignment though. We discuss the caution needed in interpretation of this analysis as the mean position angle of the vectors may not be the best representation of the field direction for all sources. In the sources where the field direction changes abruptly, modal averages (in reasonable bin sizes) may be more representative. Also, the polarimetry maps remain a very good way of analysing the alignment.

## ACKNOWLEDGEMENTS

The James Clerk Maxwell Telescope is operated by The Joint Astronomy Centre on behalf of the Science and Technology Facilities Council (STFC) of the United Kingdom, the Netherlands Organisation for Scientific Research, and the National Research Council of Canada. The authors acknowledge the data analysis facilities provided by the Starlink Project which is run by CCLRC on behalf of STFC. The Program ID's of the programs under which the data were obtained are: M98AU49, M99AU03, M00BU09. RC acknowledges funding from the Science Foundation Ireland, under grant 04/BRG/P02741.

## REFERENCES

- Aitken, D.K., Wright, C. M., Smith, C. H., & Roche, P. F., 1993, MNRAS, 262, 456
- Anderson, I.M., Harju, J., Knee, L.B.G. & Haikala, L.K., 1997, A&A, 321, 575
- Arquilla, R. & Goldsmith, P.F., 1984, ApJ, 279, 664
- Bally, J. & Lane, A.P. 1982, ApJ, 257, 612
- Bartkiewicz, A., Szymczak, M., Cohen, R. J. & Richards, A. M. S., 2005, MNRAS, 361, 623
- Baudry, A., Desmurs, J. F., Wilson, T. L. & Cohen, R. J., 1997, A & A, 325, 255
- Beichman, C.A., Becklin, E.E. & Wynn-Williams, C.G., 1979, ApJ, 232, L47.
- Berry, D. S. & Gledhill, T. M., 2001, Starlink User Note 233.5
- Bianchi, S., Gonçalves, J., Albrecht, M., et al. 2003, A&A, 399, 43
- Blaauw, A. Hiltner, W.A. & Johnson, H.L., 1959, Astrophysical Journal, 130, 69
- Botinelli, S., & Williams, J. P., 2004, A&A, 421, 1113
- Brand, J., Cesaroni, R., Palla, F., et al. 2001, A&A, 370, 230
- Campbell, M. F., Hoffmann, W. F., Thronson, H. A. et al., 1982, ApJ, 261, 550
- Chandrasekhar, S. & Fermi, E., 1953, ApJ, 118, 113
- Chini, R., Ward-Thompson, D., Kirk, J. M., et al., 2001, A&A, 369, 155
- Chrysostomou, A., Aitken, D. K., Jenness, T., et al. 2002, A&A, 385, 1014
- Clark, S., McCall, A., Chrysostomou, A., et al., 2000, MNRAS, 319, 337
- Comoretto, G., Palagi, F., Cesaroni, R., et al., 1990, A&AS, 84, 179
- Crutcher, R. M., Troland, T. H., Lazareff, B. et al., 1999, ApJ, 514, L121
- Curran, R.L., Chrysostomou, A., Collett, J.L., et al. 2004,

- A&A, 421, 195
- Davis, C. J., Chrysostomou, A., Matthews, H. E., Jenness, T. & Ray, T. P. 2000, *ApJ*, 530, 115
- De Pree, C.G., Rodriguez, L.F., Dickel, H.R. & Goss, W.M., 1995, *ApJ*, 447, 220
- Downes, D., Winnberg, A., Goss, W.M. & Johansson, L.E.B., 1975, *A&A*, 44, 243
- Doyon, R. & Nadeau, D., 1988, *ApJ*, 334, 883
- Evans, N.J. II, Slovak, M.H., Becklin, E.E., et al, 1981, *ApJ*, 244, 115.
- Giannakopoulou, J., Mitchell, G.F., Hasegawa, T.I., 1997, *ApJ*, 487, 346
- Gómez, J.F., Torrelles, J.M., Estalella, R., et al., 1992, *ApJ*, 397, 492
- Gómez, J.F., Sargent, A.I., Torrelles, J.M. et al., 1999, *ApJ*, 514, 287
- Gómez, Y., Rodríguez, L.F., Girart, J.M. et al., 2003, *ApJ*, 597, 414
- Greaves, J. S., Holland, W. S., Jenness, T. et al., 2003, *MNRAS*, 340, 353
- Gwinn, C.R., Moran, J.M. & Reid, M.J., 1992, *ApJ*, 393, 149
- Hartigan, P. & Lada, C.J., 1985, *ApJSS*, 59, 383
- Hartigan, P., Lada, C.J., Tapia, S. & Stocke, J., 1986, *AJ*, 92, 1155
- Harvey, P. M., Campbell, M. H., & Hoffman, W. F., 1977, *ApJ*, 211, 786
- Hasegawa, T.I. & Mitchell, G.F., 1995, *ApJ*, 451, 225
- Heitsch, F., Zweibel, E. G., Mac Low, M.-M., et al., 2001, *ApJ*, 561, 800
- Hildebrand, R. H., 1983, *QJRAS*, 24, 267
- Hofner, P., Cesaroni, R., Olmi, L., et al., 2007, *A&A*, 465, 197
- Holland, W. S., Robson, E. I., Gear, W. K., et al. 1999, *MNRAS*, 303, 659
- Houde, M., Bastien, P., Peng, R. et al., 2000, *ApJ*, 536, 857
- Hughes, V.A. & Waterlout, J.G.A., 1984, *Astrophysical Journal*, 276, 204
- Hutawarakorn, B. & Cohen, R.J., 2005, *MNRAS*, 357, 338
- Jenness, T., Scott, P.F. & Padman, R., 1995, *MNRAS*, 276, 1024
- Jenness, T. & Lightfoot, J. F., 1998, *ASP conference series*, Vol. 145, eds. R. Albrecht, R. N. Hook & H. A. Bushouse, p216.
- Jenness, T., Stevens, J. A., Archibald, E. N., et al., 2002, *MNRAS*, 336, 14
- Kameya, O., Hasegawa, T.I, Hirano, N., et al, 1989, *ApJ*, 339, 222
- Kastner, J. H., Weintraub, D., A. & Aspin, C., 1992, *ApJ*, 389, 357
- Kastner, J. H., Weintraub, D., A., Snell, R. L., Sandell, G., Aspin, C., Hughes, D. H., & Baas, F., 1994, *ApJ*, 425, 695
- Knapp, G.R., & Brown, R.L., 1976, *ApJ*, 199, 79
- Koppelaar, K., van Duinen, R.J., Aalders, J.W., et al, 1979, *A&A*, 75, L1
- Lada, C.J. Blitz, L., Reid, M.J., & Moran, J.M., 1981, *ApJ*, 243, 769.
- Lai, S.-P., Velusamy, T., & Langer, W. D., 2003a, *ApJ*, 596, L239
- Lai, S.-p., Girtart, J. M. & Crutcher, R. M., 2003b, *ApJ*, 598, 392
- Lebron, M., Beuther, H., Schilke, P. & Stanke, Th., 2006, *A&A*, 448, 1037
- Lenzen, R. Hodapp, K.W. & Solf, J., 1984, *A&A*, 137, 202
- Lenzen, R., 1988, *A&A*, 190, 269.
- Little, L.T., Bergman, P., Cunningham, C.T., et al., 1988, *A&A*, 205, 129-134
- Mangum, J. G., Wootten, A. & Mundy, L. G., 1991, *ApJ*, 378, 576
- Mangum, J. G., Wootten, A. & Mundy, L. G., 1992, *ApJ*, 388, 467
- Marraco, H.G. & Rydgren, A.E., 1981, *AJ*, 86, 62
- Martí, J., Rodríguez, L.F. & Reipurth, B., 1993, *ApJ*, 416, 208
- Martí, J., Rodríguez, L.F. & Torrelles, J. M., 1999, *A&A*, 345, 5
- Matthews, B. C. & Wilson, C., D. 2002, *ApJ*, 571, 356
- Mayo, E. A. Sarma, A. P., Troland, T. H. & Abel, N. P., 2004, *AAS*, 205, 9907
- McCutcheon, W. H., Sato, T., Purton, C. R., et al., 1995, *AJ*, 110, 1762
- Meakin, C. A., Hines, D. C. & Thompson, R. I., 2005, *ApJ*, 634, 1146
- Ménard, F. & Duchêne, G., 2004, *A&A*, 425, 973
- Menten, K. M. & van der Tak, F. F.S., 2004, *A&A*, 414, 289
- Merrill, K.M. & Soifer, B.T., 1974, *ApJ*, 189L, 27
- Mestel, L., 1999, *Stellar Magnetism*, International Series of Monographs on Physics, Oxford Science Publications.
- Migenes, V. Cohen, R.J. & Brebner, G.C., 1992, *MNRAS*, 254, 501
- Minchin, N.R., Hough, J.H., Burton, M.G. & Yamashita, T., 1991, *MNRAS*, 251, 522
- Minchin, N.R., White, G. J. & Ward-Thompson, D., 1995, *A&A*, 301, 894
- Momose, M., Tamura, M., Kameya, O., et al., 2001, *ApJ*, 555, 855
- Mouschovias, T., 1976, *ApJ*, 207, 141
- Mozurkewich, D., Schwartz, P.R. & Smith, H.A., 1986, *ApJ*, 311, 371
- Narayanan, G. & Walker, C. K., 1996, *ApJ*, 466, 844
- Neckel, T., 1978, *A&A*, 69, 51
- Nutter, D., Ward-Thompson, D. & André, P., 2006, *MNRAS*, 368, 1833
- Ossenkopf, V. & Henning, Th., 1994, *A&A*, 291, 943
- Ostriker, E.C., Stone, J.M. & Gammie, C.F. 2001, *ApJ*, 546, 980
- Patel, N. A., Curiel, S., Sridharan, T. K., Zhang, Q., Hunter, T., R., et al., 2005, *Natur.* 437, 109
- Preibisch, T. & Smith, M.D., 2002, *A&A*, 383, 540
- Racine, R., & van de Bergh, S., 1970, in *IAU Symp. 38, The Spiral Structure of Our Galaxy*, ed. W. Becker & G. Contopoulos (Dordrecht: Reidel), 219
- Rodríguez, L. F., Moran, J.M., Ho, P.T.P., & Gottlieb, E.W., 1980, *ApJ*, 235, 845
- Sandell, G., 1999, *A&A*, 343, 281
- Sandell, G. & Weintraub, D. A., 2001, *ApJ*, 134, 115
- Sarma, A.P., Troland, T.H., Roberts, D.A. & Crutcher, R.M., 2000, *ApJ*, 533, 271
- Sarma, A. P., Troland, T. H. & Romney, J. D., 2001, *ApJ*, 554, L217
- Scoville, N.Z., Sargent, A.I., Sanders, D.B., et al., 2000, *ApJ*, 303, 416
- Shepherd, D.S., Yu, K.C., Bally, J. & Testi, L., 2000, *ApJ*,

- 555, 833.
- Shirley, Y. L., Evans, N. J. II., Young, K. E., Knez, C. & Jaffe, D. T., 2003, *ApJS*, 149, 375
- Smith, L. F., Mezger, P. G., & Biermann, P. 1978, *A&A*, 66, 65
- Sparks, W. B. & Axon, D. J., 1999, *PASP*, 111, 1298
- Sridharan, T.K., Beuther, H., Schilke, P., et al. 2002, *ApJ*, 566, 931
- Stecklum, B., Feldt, M., Richichi, A., et al. 1997, *ApJ*, 479, 339
- Thompson, M. A., Hatchell, J., MacDonald, G., & Millar, T., 2002, in *Hot Star Workshop III: The Earliest stages of Massive Star Birth*. ASP Conference Proceedings, Vol. 267 Ed. P. Crowther, San Francisco, Astronomical Society of the Pacific, 2002, p. 429
- Thronson, H. A., Gatley, I., Harvey, P. M., et al., 1980, *ApJ*, 237, 66
- Umemoto, T., Saito, M., Yang, J. & Hirano, N., 2000, *Proceedings of the 23rd ESLAB symposium*, Eds. F. Favata, A. Kaas & A. Wilson, ESA SP, 445, 531
- Vallée, J. P. & Fiege, J. D., 2006, *ApJ*, 636, 332
- van der Tak, F. F. S., van Dishoek, E. F., Evans II, N. J. & Blake, G. A., 2000, *ApJ*, 537, 283
- Visser, A. E., Richer, J. S. & Chandler, C., J., 2002, *AJ*, 124, 2756
- Vlemmings, W. H. T., Diamond, P. J., van Langevelde, H. J. & Torrelles, J. M., 2006, *A&A*, 448, 597
- Walker, C.K., Lada, C.J. & Hartigan, O., 1985, *BAAS*, 16, 998
- Weigelt, G., Preibisch, T., Schertl, D., et al., 2002, *A&A*, 381, 905
- Weintraub, D. A., & Kastner, J. H., 1996, *ApJ*, 458, 670
- Wendker, H.J. & Baars, J.W.M., 1974, *A&A*, 33, 157
- Wiling, B.A., Mundy, L.G., Blackwell, J.H., & Howe, J.E., 1989, *ApJ*, 345, 257
- Wood, D.O.S., & Churchwell, E., 1989, *ApJS*, 69, 831
- Woody, D. P., Scott, S. L., Scoville, N. Z., Mundy, L. G., Sargeant, A. I., Padin, S., Tinney, C. G. & Wilson, C. 1989, *ApJ*, 337, L41
- Wu, Y., Zhang, Q., Chen, H., Yang, C., Wei, Y. & Ho, P. T. P., 2005, *AJ*, 129, 330
- Xu, Y., Shen, Z.-Q., Yang, J., et al., 2006, *AJ*, 132, 20
- Yamashita, T., Sato, S., Nagata, T., et al., 1987, *A&A*, 177, 258
- Yang, J., Umemoto, T., Iwata, T. & Fukui, Y., 1991, *ApJ*, 373, 137